The Astrophysical Journal, 997:179 (16pp), 2026 February 1 https://doi.org/10.3847/1538-4357/ae1f87

JWST Observations of SN 2023ixf. I. Completing the Early Multiwavelength Picture with Plateau-phase Spectroscopy

J. M. DerKacy[1,2], C. Ashall[2,3], E. Baron[4,5], K. Medler[2,3], T. Mera[6], P. Hoeflich[6], M. Shahbandeh[1,33], C. R. Burns[7], M. D. Stritzinger[8], M. A. Tucker[9,34], B. J. Shappee[3], K. Auchettl[10,11], C. R. Angus[12,13], D. D. Desai[3], A. Do[14], J. T. Hinkle[3,35], W. B. Hoogendam[3,36], M. E. Huber[3], A. V. Payne[1], D. O. Jones[15], J. Shi[10], M. Y. Kong[3], S. Romagnoli[10], A. Syncatto[3,16], S. Moran[17], E. Fereidouni[6], P. J. Brown[18], M. Engesser[1], O. D. Fox[1], L. Galbany[19,20], E. Y. Hsiao[6], T. de Jaeger[21], S. Kumar[22], J. Lu[23], M. Matsuura[24], P. A. Mazzali[25,26], N. Morrell[27], C. M. Pfeffer[3,36], M. M. Phillips[27], A. Rest[1], S. Shiber[6], L. Strolger[1], N. B. Suntzeff[18], T. Temim[28], S. Tinyanont[29], Q. Wang[30], R. Wesson[23], S. H. Park[31], and J. Rho[32]

[1] Space Telescope Science Institute, 3700 San Martin Drive, Baltimore, MD 21218-2410, USA; jderkacy@stsci.edu
[2] Department of Physics, Virginia Tech, Blacksburg, VA 24061, USA
[3] Institute for Astronomy, University of Hawai'i at Manoa, 2680 Woodlawn Dr., Hawai'i, HI 96822, USA
[4] Planetary Science Institute, 1700 East Fort Lowell Road, Suite 106, Tucson, AZ 85719-2395, USA
[5] Hamburger Sternwarte, Gojenbergsweg 112, D-21029 Hamburg, Germany
[6] Department of Physics, Florida State University, 77 Chieftan Way, Tallahassee, FL 32306, USA
[7] Observatories of the Carnegie Institution for Science, 813 Santa Barbara Street, Pasadena, CA 91101, USA
[8] Department of Physics and Astronomy, Aarhus University, Ny Munkegade 120, DK-8000 Aarhus C, Denmark
[9] Center for Cosmology and AstroParticle Physics, The Ohio State University, 191 W. Woodruff Ave., Columbus, OH 43210, USA
[10] School of Physics, The University of Melbourne, Parkville, VIC 3010, Australia
[11] Department of Astronomy and Astrophysics, University of California, Santa Cruz, CA 95064, USA
[12] Astrophysics Research Centre, School of Mathematics and Physics, Queen's University Belfast, Belfast BT7 1NN, UK
[13] DARK, Niels Bohr Institute, University of Copenhagen, Jagtvej 128, DK-2200 Copenhagen Ø, Denmark
[14] Institute of Astronomy and Kavli Institute for Cosmology, Madingley Road, Cambridge CB3 0HA, UK
[15] Institute for Astronomy, University of Hawai'i, 640 N. A'ohoku Pl., Hilo, HI 96720, USA
[16] Institute for Astronomy, University of Hawai'i, 200 W Kawili St, Hilo, HI 96720, USA
[17] School of Physics and Astronomy, University of Leicester, University Road, Leicester LE1 7RH, UK
[18] George P. and Cynthia Woods Mitchell Institute for Fundamental Physics and Astronomy, Texas A&M University, Department of Physics and Astronomy, College Station, TX 77843, USA
[19] Institute of Space Sciences (ICE, CSIC), Campus UAB, Carrer de Can Magrans, s/n, E-08193 Barcelona, Spain
[20] Institut d'Estudis Espacials de Catalunya (IEEC), E-08034 Barcelona, Spain
[21] LPNHE, (CNRS/IN2P3, Sorbonne Université, Université Paris Cité), Laboratoire de Physique Nucléaire et de Hautes Énergies, 75005, Paris, France
[22] Department of Astronomy, University of Virginia, 530 McCormick Road, Charlottesville, VA 22904, USA
[23] Department of Physics & Astronomy, Michigan State University, East Lansing, MI, USA
[24] Cardiff Hub for Astrophysical Research and Technology (CHART), School of Physics and Astronomy, Cardiff University, The Parade, Cardiff CF24 3AA, UK
[25] Astrophysics Research Institute, Liverpool John Moores University, UK
[26] Max-Planck-Institut für Astrophysik, Karl-Schwarzschild Straße 1, 85748 Garching, Germany
[27] Las Campanas Observatory, Carnegie Observatories, Casilla 601, La Serena, Chile
[28] Department of Astrophysical Sciences, Princeton University, Princeton, NJ 08544, USA
[29] National Astronomical Research Institute of Thailand, 260 Moo 4, Donkaew, Maerim, Chiang Mai 50180, Thailand
[30] Department of Physics and Kavli Institute for Astrophysics and Space Research, Massachusetts Institute of Technology, 77 Massachusetts Avenue, Cambridge, MA 02139, USA
[31] Department of Physics and Astronomy, Seoul National University, Gwanak-ro 1, Gwanak-gu, Seoul, 08826, Republic of Korea
[32] SETI Institute, 339 Bernardo Ave., Ste. 200, Mountain View, CA 94043, USA
Received 2025 July 24; revised 2025 September 30; accepted 2025 October 16; published 2026 January 21

Abstract

We present and analyze panchromatic (0.35–14 μm) spectroscopy of the Type II supernova 2023ixf, including near- and mid-infrared spectra obtained 33.6 days after explosion during the plateau phase, with the James Webb Space Telescope (JWST). This is the first in a series of papers examining the evolution of SN 2023ixf with JWST during the initial 1000 days after explosion and monitoring the formation and growth of molecules and dust in ejecta and the surrounding environment. The JWST infrared spectra are overwhelmingly dominated by H lines, whose profiles reveal ejecta structures, including flat tops, blue notches, and red shoulders, unseen in the optical spectra. We characterize the nature of these structures, concluding that they likely result from a combination of ejecta geometry, viewing angle, and opacity effects. We find no evidence for the formation of dust precursor molecules such as carbon monoxide (CO), nor do we observe an infrared excess attributable to dust. These

[33] STScI Fellow.
[34] CCAPP Fellow.
[35] FINNEST FI.
[36] NSF Graduate Research Fellow.

observations imply that the detections of molecules and dust in SN 2023ixf at later epochs arise either from freshly synthesized material within the ejecta or circumstellar material at radii not yet heated by the supernova at this epoch.

Unified Astronomy Thesaurus concepts: Core-collapse supernovae (304); Type II supernovae (1731); Supernovae (1668); James Webb Space Telescope (2291)

Materials only available in the online version of record: data behind figures

1. Introduction

Nearby supernovae (SNe) provide valuable insight into the late stages of stellar evolution and explosion physics, which cannot be replicated by observations of more distant objects. Their proximity enables earlier detection and long-duration follow-up campaigns, detailed studies of the surrounding environment, and (when data exist) investigation of the pre-explosion nature of the progenitor star.

SN 2023ixf was discovered in Messier 101 (M101, $d = 6.85$ Mpc) on 2023 May 19.73 UT (MJD = 60083.73) by Kōichi Itagaki (K. Itagaki 2023). Rapid spectroscopic observations revealed SN 2023ixf to be a Type II supernova (SN II) with multiple flash ionization features (D. Perley & A. Gal-Yam 2023). Due to the rarity of SNe at $d < 7$ Mpc, a global, ground- and space-based follow-up campaign constrained early-time physics of the explosion spanning γ-ray (E. Ravensburg et al. 2024; P. Sarmah 2024), X-ray (B. W. Grefenstette et al. 2023; P. Chandra et al. 2024; S. Panjkov et al. 2024; A. J. Nayana et al. 2025), ultraviolet (G. Hosseinzadeh et al. 2023; R. S. Teja et al. 2023; K. A. Bostroem et al. 2024; E. A. Zimmerman et al. 2024), optical (K. A. Bostroem et al. 2023; D. Hiramatsu et al. 2023; G. Hosseinzadeh et al. 2023; W. V. Jacobson-Galán et al. 2023; N. Smith et al. 2023; M. Stritzinger et al. 2023; M. Yamanaka et al. 2023; P. D. Michel et al. 2025), near-infrared (NIR; M. Yamanaka et al. 2023; S. D. Van Dyk et al. 2024a; S. H. Park et al. 2025), and radio (E. Berger et al. 2023; Y. Iwata et al. 2025) wavelengths. Upper limits on multimessenger signals from neutrinos (D. Guetta et al. 2023; A. Kheirandish & K. Murase 2023) and gravitational waves (A. G. Abac et al. 2025) were also studied.

SN 2023ixf is a rapidly declining SN II ($s_2 = 1.85$ mag (100 days)$^{-1}$)[37] whose peak luminosity is enhanced by circumstellar interaction (K. A. Bostroem et al. 2024; A. Singh et al. 2024; E. A. Zimmerman et al. 2024). The structure of this circumstellar material is multifaceted, comprising an outer, low-density region (K. A. Bostroem et al. 2024), and an inner region of enhanced mass loss ejected in the final few years before the explosion (K. A. Bostroem et al. 2024; Y. Iwata et al. 2025), which may be disk-like or toroidal in shape (S. S. Vasylyev et al. 2023; A. Singh et al. 2024). The completeness of these early data has enabled detailed modeling of the progenitor, its surroundings, and the early light curve, including shock breakout (Z. Niu et al. 2023; N. Soker 2023; J. Zhang et al. 2023; M. C. Bersten et al. 2024; G. Li et al. 2024; L. Martinez et al. 2024; T. J. Moriya & A. Singh 2024; M. Hu et al. 2025).

The proximity of SN 2023ixf also enabled searches for both pre-explosion variability and direct detection of the progenitor in archival images of both ground- and space-based telescopes from the ultraviolet through mid-infrared (MIR; Y. Dong et al. 2023; N. Flinner et al. 2023; C. D. Kilpatrick et al. 2023). While there is consensus that the progenitor star was a dusty red supergiant (RSG), estimates of the progenitor mass cover both the low-mass end ($M \lesssim 12\ M_\odot$; C. D. Kilpatrick et al. 2023; J. L. Pledger & M. M. Shara 2023; J. M. M. Neustadt et al. 2024; S. D. Van Dyk et al. 2024b) and the high-mass end ($M \gtrsim 17\ M_\odot$; J. E. Jencson et al. 2023; C. Liu et al. 2023; Z. Niu et al. 2023; M. D. Soraisam et al. 2023; Y.-J. Qin et al. 2024; C. L. Ransome et al. 2024) of plausible SN II progenitors (S. J. Smartt 2015).

Early observations at IR wavelengths are crucial for understanding the formation of molecules and dust in SNe II. Much of the dust observed in the early Universe (F. Bertoldi et al. 2003; R. Maiolino et al. 2004; E. Dwek et al. 2007; Q. Li et al. 2020) is thought to have formed in the ejecta of core-collapse SNe (F. Cernuschi et al. 1967; F. Hoyle & N. C. Wickramasinghe 1970). This is because the asymptotic giant branch stars that produce this dust in the local Universe are not yet old enough to have produced the observed dust masses in these high-z galaxies (E. Dwek 1998; A. S. Ferrarotti & H. P. Gail 2006; C. Gall et al. 2011; M. Di Criscienzo et al. 2013; F. Dell'Agli et al. 2015). The formation of molecules in the SN ejecta provides both an important cooling mechanism and the necessary nucleation sites for the later formation and survival of dust grains.

The most prominent of these molecules in the NIR and MIR wavelengths are carbon monoxide (CO) and silicon monoxide (SiO). The timing, location, and amount of CO and SiO formation are related to the He-core mass of the progenitor, which determines the relative conditions and abundances within the progenitor star at the time of explosion (S. E. Woosley et al. 2002; A. Sarangi & I. Cherchneff 2013; B. Müller et al. 2016; E. S. Brooker et al. 2022; L. Dessart 2025). SNe II progenitors from systems with strong binary interaction (e.g., mergers) may have different He-core masses than those from single-star systems (E. Zapartas et al. 2021; D. Tsuna et al. 2025). CO and/or SiO have been detected in SN 1987A (R. M. Catchpole et al. 1988; J. Spyromilio et al. 1988; W. P. S. Meikle et al. 1989; D. H. Wooden et al. 1993), multiple SNe II observed by the Spitzer Space Telescope (e.g., R. Kotak et al. 2006; T. Szalai & J. Vinkó 2013), and well-studied SNe II with ground-based NIR time series (e.g., R. Kotak et al. 2005; O. D. Fox et al. 2010; J. Rho et al. 2018; S. Davis et al. 2019; T. Szalai et al. 2019). The first overtone of CO has been detected in ground-based NIR spectroscopy of SN 2023ixf starting +199 days after explosion (S. H. Park et al. 2025). Both the first overtone and the CO fundamental have been detected in time-series James Webb Space Telescope (JWST) spectroscopy spanning ~250–720 days (K. Medler et al. 2025a). Recent JWST observations of the most nearby SNe II demonstrate the ability of CO to trace the formation and evolution of dust over decades (O. C. Jones et al. 2023; J. Larsson et al. 2023; M. Shahbandeh et al. 2023, 2025). These long-baseline observations are critical for

[37] s_2 is defined by J. P. Anderson et al. (2014) as the decline rate in V-band magnitude per 100 days during the "plateau" phase.

Table 1
Properties of SN 2023ixf and Messier 101

Parameter	Value	Source
SN 2023ixf		
R.A.	$14^h03^m38\overset{s}{.}562$	(1)
Decl.	$+54°18'41\overset{''}{.}94$	(1)
Discovery (MJD)	60083.73	(2)
T_{exp} (MJD)	60082.75	(3)
V_{max} (mag)	~ -18.4	(4)
$E(B-V)_{MW}$ (mag)	0.0077 ± 0.0002	(5)
$E(B-V)_{Host}$ (mag)	0.031 ± 0.012	(6)
Messier 101		
R.A.	$14^h03^m12\overset{s}{.}544$	(7)
Decl.	$+54°20'56\overset{''}{.}22$	(7)
Morphology	SAB(rs)cd	(8)
v_{helio} (km s^{-1})	241 ± 2	(7)
v_{rot} (km s^{-1})	7 ± 1	(6)
z	0.000804	(9)
μ	29.18 ± 0.04	(9)
d_L (Mpc)	6.85 ± 0.15	(9)

References. (1) Transient Name Server; (2) K. Itagaki (2023); (3) G. Hosseinzadeh et al. (2023); (4) E. A. Zimmerman et al. (2024); (5) E. F. Schlafly & D. P. Finkbeiner (2011); (6) N. Smith et al. (2023); (7) NASA/IPAC Extragalactic Database; (8) G. de Vaucouleurs et al. (1991); (9) A. G. Riess et al. (2022)

determining how the dust mass grows over time in SNe II (C. Gall et al. 2014; E. Dwek et al. 2019), but rely on the upper limits of surviving molecules and dust in both the nearby circumstellar medium (CSM) and the interstellar medium determined at early times.

Long-baseline observations are especially important for understanding dust formation in SNe II with dense CSM (e.g., SNe IIL/P with early flash features) or SNe II that show long-lived interaction (e.g., SNe IIn). The shocks that form as a result of the interaction between the ejecta and the CSM can destroy interstellar dust through evaporative collisions between grains and thermal sputtering (M. J. Barlow 1978a, 1978b, 1978c; A. P. Jones et al. 1996; A. P. Jones 2004; J. D. Slavin et al. 2015, 2020). However, these shocks are also responsible for forming the cold dense shell (CDS), the most likely site of new dust formation within the SN ejecta (M. Pozzo et al. 2004; W. P. S. Meikle et al. 2011). Dust may also form in the surrounding dense CSM (N. Smith et al. 2008; A. A. Miller et al. 2010), and preexisting dust grains may serve as condensation sites for additional dust growth (O. D. Fox et al. 2010, 2011). Distinguishing between these sources of dust is important to understanding how shocks influence dust formation (C. Gall et al. 2014; M. Matsuura et al. 2019) and whether SNe IIn are more likely to form dust with different characteristics than other subsets of SNe II (e.g., M. Pozzo et al. 2004; N. Smith et al. 2009; D. B. Serrano-Hernández et al. 2025).

Here, we present plateau-phase JWST spectra of the nearby SN 2023ixf obtained with the Near-Infrared Spectrograph (NIRSpec; P. Jakobsen et al. 2022; T. Böker et al. 2023) and the Low Resolution Spectrograph (LRS; S. Kendrew et al. 2015) of the Mid-Infrared Instrument (MIRI), and contemporaneous ground-based spectral observations in the optical and NIR. This is the first paper in a series of papers documenting the evolution of SN 2023ixf with JWST spectroscopy obtained by the MidInfraRed SuperNovA Collaboration (MIRSNAC) under programs JWST-DD-4522 (C. Ashall et al. 2023a), JWST-DD-4575 (C. Ashall et al. 2023b), and JWST-GO-5290 (C. Ashall et al. 2024). Paper II (K. Medler et al. 2025a) focuses on the panchromatic evolution and NIR+MIR spectroscopic properties of SN 2023ixf during the nebular phase. The observations presented here and in Paper II lay the groundwork for future efforts to model the full panchromatic spectral energy distribution (SED) and emission-line properties. Scheduled observations in upcoming cycles will (when combined with this dataset) offer unprecedented insight into the location and conditions under which molecules and dust form in SNe II, and set the stage for continued observations of SN 2023ixf throughout the lifetime of JWST.

In Section 2, we present our observations and reduction procedures. We identify the strong lines in the spectrum in Section 3, and compare them to previous IR observations in Section 4. We discuss the overall SED in Section 5, while Section 6 analyzes the velocities and profiles of the identified features. Section 7 showcases our modeling efforts, including placing limits on the amount of dust precursor molecules present in the ejecta. We summarize our findings in Section 8.

2. Observations

2.1. JWST Observations

Observations of SN 2023ixf with JWST were obtained through our program DD-JWST-4522 (C. Ashall et al. 2023a), using both NIRSpec and MIRI/LRS beginning at 2023 June 21.33 UT. Consistent with other works, we adopt an explosion time of MJD = 60082.75 as derived from the midpoint of the earliest reported detection and the latest deep nondetection (G. Hosseinzadeh et al. 2023; Y. Mao et al. 2023; O. Yaron et al. 2023; E. A. Zimmerman et al. 2024). This places our JWST observations +33.6 days after explosion. Key properties related to SN 2023ixf and its host galaxy M101 used throughout this paper are summarized in Table 1. NIRSpec observations were performed with the F170LP/G235M ($\sim$1.66–3.07 μm) and F290LP/G395M ($\sim$2.87–5.10 μm) filter/grating combinations, providing continuous coverage from 1.7 to 5.1 μm at $R \sim 1000$. MIRI/LRS observations span the $\sim$5–14 μm range at a wavelength-dependent resolution $R \approx 50$–200. The data were reduced using the JWST Science Calibration Pipeline (v1.18.0; H. Bushouse et al. 2025) and CRDS version `jwst_1364.pmap`. These data can be accessed via doi:10.17909/ekjp-5b33. Full details of the observational setup are provided in Table 2.

2.2. Ground-based Observations

Ground-based follow-up observations of SN 2023ixf at optical and NIR wavelengths were obtained to complete the spectral energy distribution. Optical spectroscopic follow-up observations spanning 2.60–64.57 days after explosion were made with both the Supernova Integral Field Spectrograph (SNIFS; B. Lantz et al. 2004) on the University of Hawai'i 88 in telescope (UH88) and the Alhambra Faint Object Spectrograph and Camera (ALFOSC) on the 2.5 m Nordic Optical Telescope (NOT). UH88 spectra were obtained by the Spectroscopic Classification of Astronomical Transients collaboration (SCAT; M. A. Tucker et al. 2022). These data were reduced following the methods

Table 2
Observation Details

Parameter	Value	Value
NIRSpec Acquisition Image		
Filter	F140X	
Exposure Time (s)	0.08	
Readout pattern	NRSRAPID	
NIRSpec Spectral Observations		
Slit	S400A1	
Subarray	SUBS400A1	
Grating/filter	G235M/F170LP	G395M/F290LP
T_{obs} (MJD)	60116.34	60116.33
Phase from exposure (days)	+33.58	+33.57
Exposure time (s)	60.8	98.2
Groups per integration	3	5
Integrations per exposure	1	1
Exposures per dither	1	1
Total dithers	3	3
Readout pattern	NRS	NRS
MIRI Acquisition Image		
Filter	F560W	
Exposure time (s)	11.1	
Readout pattern	FAST	
MIRI Spectral Observations		
Mode	LRS	
Exposure time (s)	260.9	
T_{obs} (MJD)	60116.35	
Phase from exposure (days)	+33.59	
Groups per integration	15	
Integrations per exposure	3	
Exposures per dither	1	
Total dithers	2	
Ground-based Optical Spectra		
Telescope	NOT	
Instrument	ALFOSC	
T_{obs} (MJD)	60117.08	
Phase from exposure (days)	+34.32	
Exposure time (s)	180	
Ground-based NIR Spectra		
Telescope	IRTF	
Instrument	Spex	
T_{obs} (MJD)	60115.48	
Phase from exposure (days)	+32.72	
Exposure time (s)	169.6	

outlined by M. A. Tucker et al. (2022). NOT spectroscopic observations were obtained as part of a follow-up campaign of SN 2023ixf led by the NOT Unbiased Transient Survey (NUTS2).[38] The data were reduced following standard methods; including bias subtraction, flat-fielding of the two-dimensional images, wavelength calibration of the extracted spectrum from arc lamp exposures, and the removal and correction of telluric features and cosmic rays. Three individual, 180 s exposures with high signal-to-noise ratio (S/N) were obtained and median-combined. The midpoint of the three exposures (MJD = 60117.08; +34.32 days) is adopted as the time of the observation.

NIR time-series spectra of SN 2023ixf were obtained by HISS (K. Medler et al. 2025b) between +8.58 and +32.72 days from the explosion with Keck II/NIRES and Infrared Telescope Facility (IRTF)/SpeX. Details on the instrument configurations and associated reduction procedures are given by K. Medler et al. (2025b).

For the purposes of constructing a contemporaneous panchromatic SED spanning the optical to MIR, we combine the NOT optical spectra obtained on MJD = 60117.08 and the IRTF spectra from MJD = 60115.48 with our JWST data. A full log of the ground-based observations can be found in Table 3.

Table 3
Log of Spectroscopic Observations

Date (UT)	MJD	Epoch[a]	Exp. Time (s)
UH88/SNIFS Optical Spectra			
2023 May 21.34	60085.34	2.59	2000
2023 May 23.25	60087.25	4.52	2000
2023 May 25.34	60089.34	6.61	1800
2023 Jun 04.41	60099.41	16.68	1800
2023 Jun 05.25	60100.25	17.54	1800
2023 Jun 10.44	60105.44	22.69	1800
2023 Jun 12.44	60107.44	24.69	1800
2023 Jun 16.33	60111.33	28.59	1800
2023 Jun 20.29	60115.29	32.55	1800
2023 Jun 24.30	60119.30	36.56	1800
2023 Jun 26.28	60121.28	38.55	1800
2023 Jun 28.27	60123.27	40.53	1800
2023 Jun 30.29	60125.29	42.56	1800
2023 Jul 04.41	60129.41	46.66	1800
2023 Jul 06.43	60131.43	48.68	1800
2023 Jul 08.29	60133.29	50.55	1800
2023 Jul 10.29	60135.29	52.55	2400
2023 Jul 12.29	60137.29	54.56	1800
2023 Jul 14.26	60139.26	56.53	1800
2023 Jul 16.28	60141.28	58.54	1800
2023 Jul 22.31	60147.31	64.57	1800
Near-infrared Spectra			
2023 May 27.33	60091.33	8.58	40
2023 Jun 04.24	60099.24	16.49	3415.82
2023 Jun 06.24	60101.24	18.49	5213.62

Note.
[a] Rest-frame days relative to explosion on MJD = 60082.75 (G. Hosseinzadeh et al. 2023).

3. Line Identifications

Figure 1 shows the lines identified in the combined spectra of SN 2023ixf, with the individual transitions listed in Table 4. These identifications were compiled from a list of plausible lines seen in previous analyzes of SNe II, including: P. A. Mazzali et al. (1992), E. Baron et al. (2003), C. P. Gutiérrez et al. (2017), S. Davis et al. (2019), M. Shahbandeh et al. (2022, 2024), and sources therein.

Similar to the JWST observations of SN 2022acko (M. Shahbandeh et al. 2024), the spectra during the plateau phase are dominated by strong hydrogen lines from the

[38] https://nuts.sn.ie/

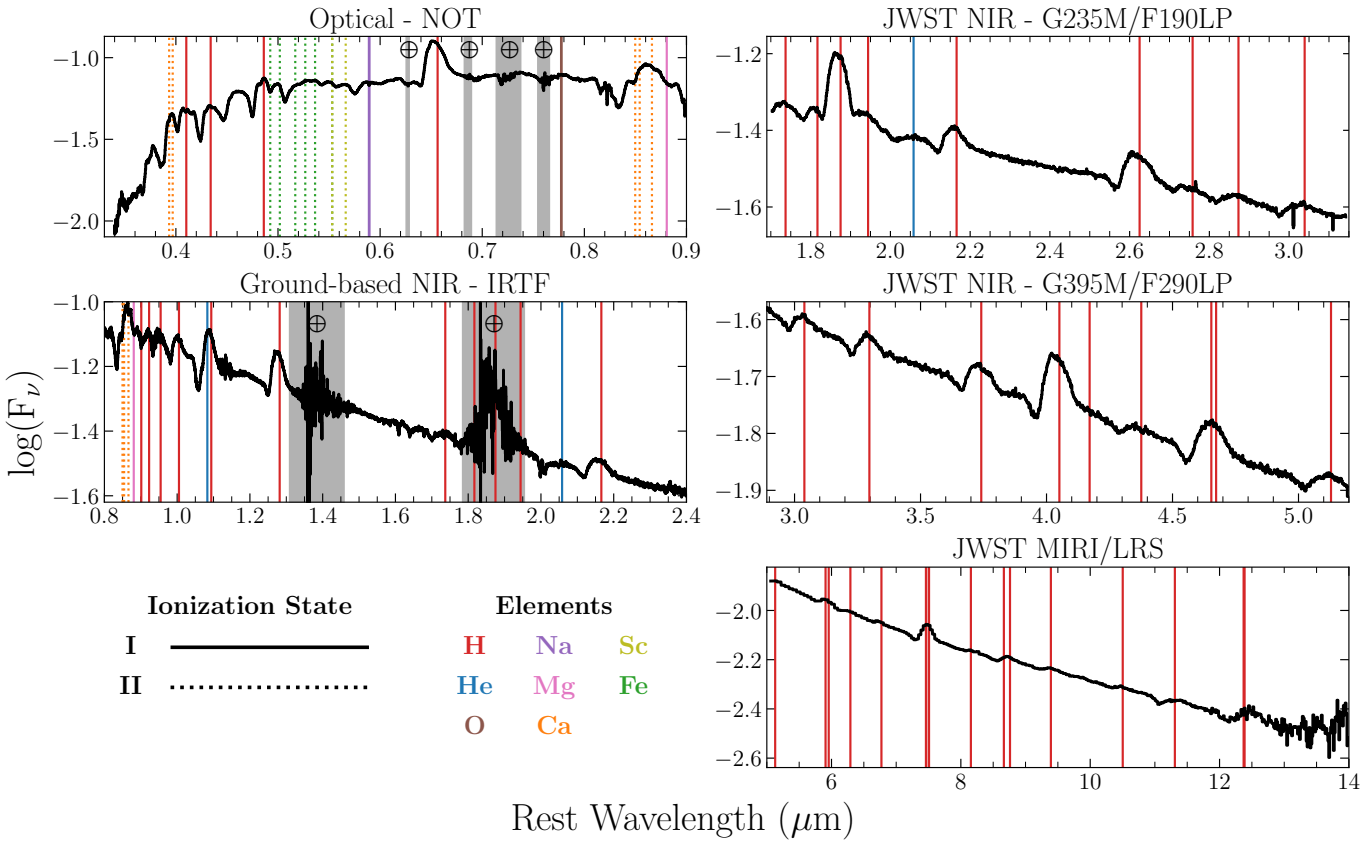

Figure 1. Line identifications based on known transitions common to SNe II (see Table 4). The spectra shown are arranged by telescope and grating combination. Based on Monte Carlo fits (see Section 6.1), the absorption troughs are shifted by up to -7500 km s^{-1} for hydrogen lines and ~ -6100 km s^{-1} for all other lines. Strong telluric regions in the ground-based optical and NIR data are marked in gray.

Balmer, Paschen, Brackett, Pfund, Humphreys, and other unnamed higher-order series. Strong lines (e.g., the α, β, and γ transitions) within the named H series appear with well-defined P Cygni shapes. Weaker lines (e.g., the ϵ, ζ, and η transitions) show a larger diversity in their line profiles, often appearing with weaker relative emission components or only in absorption. E. Baron et al. (2025) find similar behavior in both their observations and non-LTE (NLTE) model of SN 2024ggi, and discuss what ejecta conditions lead to the formation of the different line profiles. In the line identifications presented below, we consider weaker hydrogen lines as identified components of blends if: (1) another strong line originating from the same upper energy state is seen elsewhere in the spectrum, or (2) if an additional line from the same series originating in a higher energy level is clearly seen (e.g., as in the case of Huγ).

3.1. NIRSpec (1.7–5 μm)

The combined NIR spectrum is primarily dominated by H lines of the Brackett, Pfund, and Humphreys series, all of which have remarkably similar P Cygni profiles. The identified lines include: Brζ (1.737 μm), Brϵ (1.817 μm), Paα (1.875 μm), Brδ (1.944 μm), Brγ (2.166 μm), Brβ (2.626 μm), Pfθ (2.675 μm), Pfη (2.758 μm), Pfζ (2.873 μm), Pfϵ (3.039 μm), Pfδ (3.297 μm), Pfγ (3.741 μm), Brα (4.052 μm), Huη (4.171 μm), Huζ (4.376 μm), Pfβ (4.654 μm), Huϵ (4.673 μm), and Huδ (5.129 μm).

There is an additional weak, broad feature near 2.05 μm, which we tentatively identify as the He I 2.0581 μm line. This identification is supported by the presence of the He I 1.083 μm line in the ground-based NIR data (see Section 3.4) despite the lack of strong He lines at the optical wavelengths. This is consistent with the optical He lines being more difficult to excite than those in the NIR (R. P. Harkness et al. 1987; L. B. Lucy 1991).

At this phase, there is no evidence for CO emission from either the fundamental ($\sim$4.2–6 μm) or first overtone ($\sim$2.1–2.6 μm) rovibrational bands. Upper limits on the amount of CO are further explored in Section 7. See S. H. Park et al. (2025) and K. Medler et al. (2025a) for discussions on the detection of CO at later phases in SN 2023ixf.

3.2. MIRI/LRS (5–14 μm)

In the MIR spectrum, two features are particularly strong. The first is the blend of Pfα (7.459 μm) and Huβ (7.502 μm); the second is the Huα (12.372 μm) line, which itself is weakly blended with H I (8–11) (12.387 μm). Based on the detection of Huδ in both the LRS and NIRSpec data, we identify the Huγ (5.908 μm) line, albeit with a significantly undersampled and possibly blended profile.

Identification of additional features becomes more difficult as the strength of the features above the continuum decreases. Furthermore, the low resolution of the spectrograph ($R \approx 50$–200) undersamples the line profiles by spreading them over only a small handful (2–5) of pixels. When combined with the different line profile shapes found in MIR models of SNe II (E. Baron et al. 2025), the observed line profiles may appear different for lines that should otherwise appear nearly identical. This can be clearly seen

Table 4
Line Identifications

Line	Wavelength (μm)	Line	Wavelength (μm)
Optical Lines (0.35–0.9 μm)			
Ca II	0.3934	Fe II	0.5531
Ca II	0.3968	Sc II	0.5531
H I (Hδ)	0.4102	Sc II	0.5663
Fe II	0.4303	Na I	0.5983
H I (Hγ)	0.4340	H I (Hα)	0.6563
H I (Hβ)	0.4861	O I	0.7774
Fe II	0.4924	Ca II	0.8498
Fe II	0.5018	Ca II	0.8542
Fe II	0.5169	Ca II	0.8662
Fe II	0.5267	Mg I[a]	0.8807
Fe II	0.5363	H I (Paη)	0.9014
Ground-based NIR Lines (0.9–1.7 μm)			
H I (Paζ)	0.923	He I	1.083
H I (Paϵ)	0.955	H I (Paγ)	1.094
H I (Paδ)	1.005	H I (Paβ)	1.282
NIRSpec Lines (1.7–5 μm)			
H I (Brζ)	1.737	H I (Pfϵ)	3.039
H I (Brϵ)	1.817	H I (Pfδ)	3.297
H I (Paα)	1.875	H I (Pfγ)	3.741
H I (Brδ)	1.944	H I (Brα)	4.052
He I[a]	2.058	H I (Huη)	4.171
H I (Brγ)	2.166	H I (Huζ)	4.376
H I (Brβ)	2.626	H I (Pfβ)	4.654
H I (Pfθ)	2.675	H I (Huϵ)	4.673
H I (Pfη)	2.758	H I (Huδ)	5.129
H I (Pfζ)	2.873	…	…
MIRI/LRS Lines (5–14 μm)			
H I (Huγ)	5.908	H I (8–14)[a]	8.665
H I (7–14)[a]	5.957	H I (7–10)[a]	8.760
H I (7–13)[a]	6.292	H I (8–13)[a]	9.392
H I (7–12)[a]	6.772	H I (8–12)[a]	10.503
H I (Pfα)	7.459	H I (7–9)[a]	11.309
H I (Huβ)	7.502	H I (Huα)	12.372
H I (7–11)[a]	7.508	H I (8–11)[a]	12.387
H I (8–15)[a]	8.155	…	…

Note.
[a] Tentative.

in the Huγ line, which appears weak in both absorption and emission, compared to both the Huα line at higher resolution in the LRS data (a strong P Cygni profile) and the Huδ line (a "detached" profile with weak emission; E. Baron et al. 2025) in the NIRSpec data (see Section 6).

Relying on the spectroscopic models of a companion paper on the plateau-phase JWST spectroscopy of SN 2024ggi (E. Baron et al. 2025), we are able to tentatively identify several additional hydrogen lines. These identifications are supported by the models showing hydrogen features with similar profiles and strengths above the continuum. These lines include: H I (7–14) (5.957 μm), H I (7–13) (6.292 μm), H I (7–12) (6.772 μm), H I (7–11) (7.508 μm), H I (8–15) (8.155 μm), H I (8–14) (8.665 μm), H I (7–10) (8.760 μm), H I (8–13) (9.392 μm), H I (8–12) (10.503 μm), H I (7–9) (11.309 μm), and H I (8–11) (12.387 μm).

Beyond $\sim$13 μm, the decreased throughput of the LRS mode results in noise levels exceeding the feature strengths above the continuum, making further line identifications difficult.

3.3. Optical (0.35–0.9 μm)

The NOT optical spectrum of SN 2023ixf shows features typical of normal SNe II roughly 30 days after explosion. The spectrum displays a prominent Hα line with a defined P Cygni profile, while other Balmer lines including Hβ, Hγ, and Hδ show only absorption components, as expected at these phases (C. P. Gutiérrez et al. 2017). Other strong features identified include the Ca II H & K lines; Fe II lines at 0.4861, 0.4924, 0.5018, 0.5169, 0.5267, 0.5363, 0.5531 μm; the Na I D doublet; the Ca II NIR triplet; and Paη (0.9014 μm).

Some weaker features also appear in the optical spectrum. Tentative evidence exists for absorption from O I λ7774, but it is strongly contaminated by telluric absorption. Weak Sc II features are seen at 0.5531 μm (blended with the Fe II transition at the same wavelength) and 0.5663 μm, with absorption minima matching that of the unblended Fe II 0.5169 μm line (-6120 ± 420 km s^{-1}), which is taken to represent the photosphere. No evidence is seen for an absorption minimum corresponding to Sc II 0.6247 μm at the photospheric velocity, suggesting that the trough to the blue of the Hα P Cygni is a "Cachito" feature (C. P. Gutiérrez et al. 2017). Consistent with other works (A. Singh et al. 2024), we find the most likely origin of the Cachito in SN 2023ixf to be high-velocity (HV) Hα, based on the velocity measures described in Section 6.1.

3.4. Ground-based NIR (0.9–1.7 μm)

Ground-based NIR spectra from IRTF show good agreement with the JWST NIRSpec data; e.g., the spectrum is dominated by Paschen series lines on top of a blackbody-like continuum. In the 0.9–1.7 μm region not covered by optical data nor the JWST data, we see Paζ (0.923 μm), Paϵ (0.955 μm), Paδ (1.005 μm), Paγ (1.094 μm), and Paβ (1.282 μm). The increased strength of the absorption trough of the Paγ feature relative to those of other Paschen lines in the ground-based and JWST NIR spectra is due to the blending of the He I λ1.083 line within the feature. This identification is confirmed by the weak P Cygni He I line seen in the +8.58 days NIR spectrum prior to the emergence of strong P Cygni H lines in both the optical and NIR, and the measured velocity of the He I λ1.083 line matching that of the Paγ line (see Section 6.1 for details). These line identifications are consistent with those found in other ground-based NIR spectral time-series observations (S. H. Park et al. 2025).

The strong presence of the He I λ1.083 line further supports the identification of the weak, broad emission of the feature near 2.05 μm as He I; as the broad emission is also seen in the HISS data presented here and the ground-based NIR time-series spectra of S. H. Park et al. (2025). We note that several other potential confounding lines could contribute to such a blend, including C, Mg, Si, and Sr lines (S. Davis et al. 2019; M. Shahbandeh et al. 2022). However, we consider these lines as unlikely contributors because, if present, their velocities would be inconsistent with the measured photospheric velocity. The spectrum shows high qualitative agreement with "strong SNe II" within the scheme of S. Davis et al. (2019), and a "strong" classification is consistent with the measured value of s_2 and the absence of observed Sr II features at λ1.033

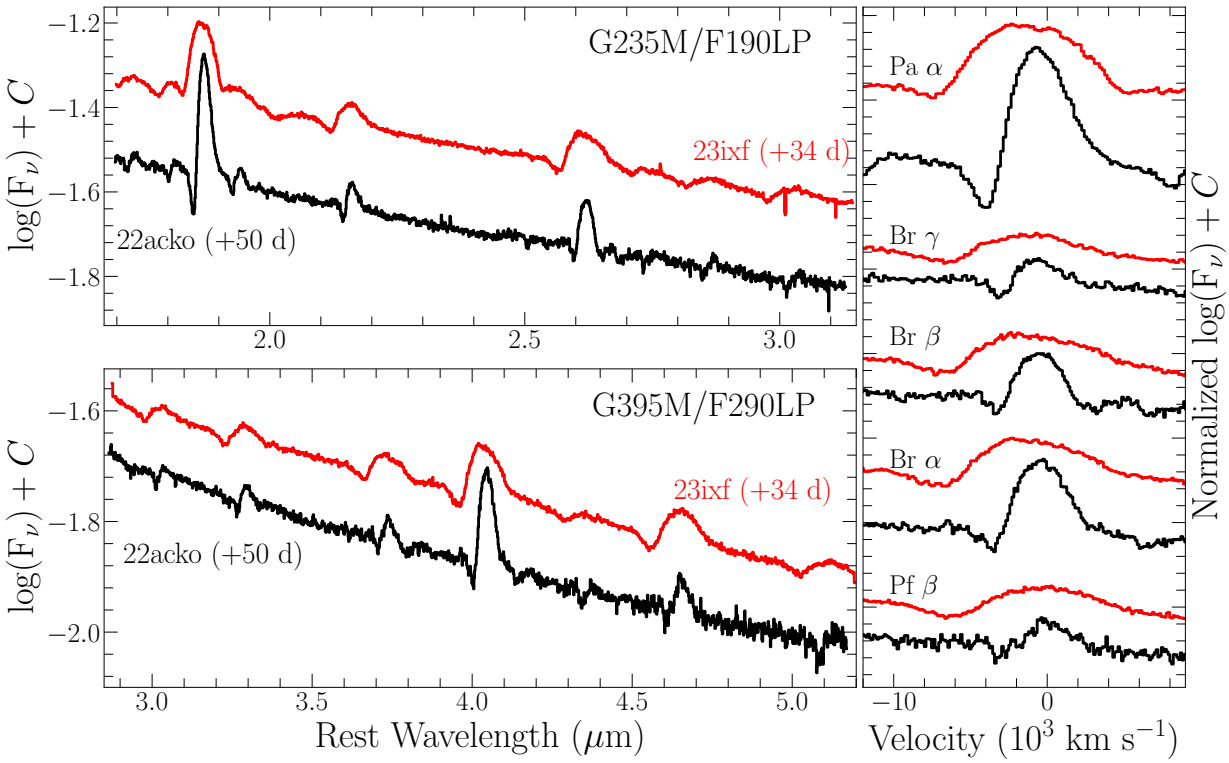

Figure 2. Comparison of SN 2023ixf to SN 2022acko NIRSpec data (left panels). The line profiles of the strongest H lines in the NIRSpec coverage (Paα, Brγ, Brβ, Brα, and Pfβ) are shown in velocity space on the right; highlighting the broader emission and weaker absorption found in SN 2023ixf relative to SN 2022acko.

μm. Such a classification is important because "strong" and "weak" SNe II show differences in both the presence of Sr II and the formation timescales of CO (S. Davis et al. 2019). Importantly, the first overtone of CO is observed as early as $\sim$100 days in other "strong" SNe II, and signals the arrival of ejecta conditions favorable for the formation of dust (C. L. Gerardy et al. 2000; S. E. Woosley et al. 2002; R. Kotak et al. 2005, 2006; S. Davis et al. 2019).

4. Comparisons to Previous MIR Observations

4.1. JWST/NIR Comparisons

Figure 2 shows the comparison of SN 2023ixf to the +50 days spectrum of SN 2022acko also taken with JWST/NIRSpec (M. Shahbandeh et al. 2024). Both spectra were obtained roughly halfway through their respective plateau phases. The spectra show the same hydrogen lines are present, with the lines appearing faster, broader, and more rounded in SN 2023ixf relative to SN 2022acko. This behavior is commonly observed in SNe II (M. Hamuy & P. A. Pinto 2002; T. de Jaeger et al. 2020), where brighter objects such as SN 2023ixf ($V_{\rm max} \approx -18.4$ mag) show higher Hβ velocities than dimmer SNe II such as SN 2022acko ($V_{\rm max} = -15.4$ mag).

4.2. MIR Comparisons

Figure 3 shows the MIR spectra of SN 2023ixf and SN 2022acko, along with MIR spectra of SNe 1987A (D. K. Aitken et al. 1988a) and 2005af (R. Kotak et al. 2006) at similar phases from explosion. We note that the Spitzer observations of SN 2005af likely occurred after it left the plateau phase (R. Kotak et al. 2006), whereas SN 1987A observations were taken during its rise to secondary maximum.

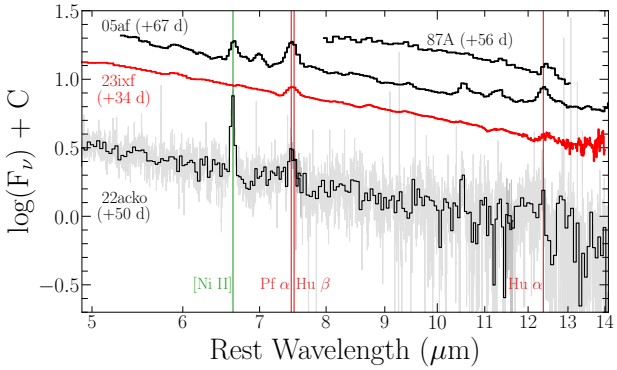

Figure 3. Comparison of SN 2023ixf MIRI/LRS data to MIR spectra of SNe 1987A (D. K. Aitken et al. 1988a), 2005af (R. Kotak et al. 2006), and 2022acko (M. Shahbandeh et al. 2024) at similar epochs, with strong lines common to multiple SNe highlighted. The SN 2022acko observations have been smoothed to $R = 200$ to better match the low-resolution data of the other observations.

The SN 2022acko spectrum presented here has been re-reduced using the `AstroBkgInterp`[39] package (B. Nickson et al. 2025, in preparation; M. Shahbandeh et al. 2025). Relative to the reduction presented by M. Shahbandeh et al. (2024), the use of `AstroBkgInterp` for the background subtraction provides a higher S/N for this observation by modeling the underlying background in each image slice independently by a two-dimensional polynomial extrapolation (in this instance with third-degree polynomials) to the background enclosed in an annulus neighboring the extraction

[39] https://github.com/brynickson/AstroBkgInterp

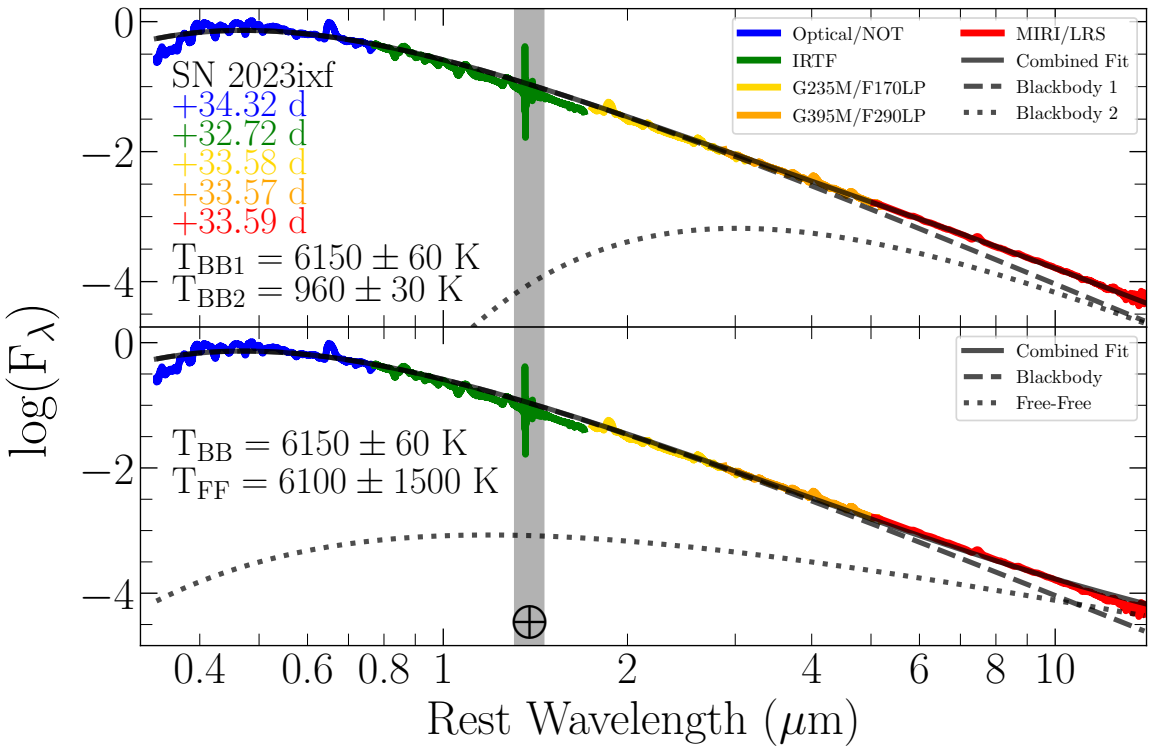

Figure 4. The optical through MIR SED of SN 2023ixf compared to the simultaneous multicomponent Monte Carlo fits. The top panel shows a fit comprising two blackbodies, while the bottom panel replaces the second, cooler blackbody with free–free emission. Both fits are able to reproduce the emission at $\lambda > 4$ μm, but are overfit according to χ^2. Based on the physical processes that are occurring in the SN ejecta, we rule out warm dust as a source of the IR excess.

aperture surrounding the SN. This modeled background is then subtracted from the `s3d` files produced by Stage 2 of the JWST Pipeline before feeding the background-subtracted data cube back into Stage 3, where the final extraction is performed channel-by-channel as normal with the `Extract1D` function.

The two strongest features are the Pfα plus Huβ blend and the Huα line, which are also seen in the other three SNe.[40] The subset of weaker (e.g., $n_l = 7$, 8 series) hydrogen lines identified in the MIR spectra varies between objects, due to instrumental sensitivities and blending.

In our new reduction of SN 2022acko narrow emission from 6.636 μm [Ni II] is now seen as it was in SN 2005af, but it is absent from SNe 1987A and 2023ixf. The 6.985 μm [Ar II] line is not detected in either SN 2022acko or SN 2023ixf, nor is it in seen in the +60 days spectrum of SN 1987A shown by D. M. Rank et al. (1988). Observations of SN 2004dj after the plateau phase (roughly +106 and +129 days after explosion) also show 6.636 μm [Ni II] and 7.50 μm [Ni I] (R. Kotak et al. 2005). The lack of forbidden emission lines in SN 2023ixf supports the conclusion that the photosphere in the IR still resides within the H-rich envelope at this phase. Observations of SN 2022acko (T. Mera et al. 2025, in preparation), SN 2023ixf (K. Medler et al. 2025a), and additional SNe II after their plateau phases with JWST will allow the community to investigate differences in the forbidden lines in the MIR.

[40] The Pfα blend in SN 1987A falls outside the wavelength range of the D. K. Aitken et al. (1988a) observations shown in Figure 3, but is clearly visible in the +60 days spectrum in Figure 1 of both D. M. Rank et al. (1988) and D. H. Wooden et al. (1993).

5. Spectral Energy Distribution

Figure 4 shows the optical through MIR SED of SN 2023ixf. The data have been corrected for extinction and redshift, and the ground-based optical and NIR spectra have been scaled to match the JWST spectra in the overlap regions. At optical and NIR wavelengths (0.4 μm $\lesssim \lambda \lesssim$ 4 μm), the underlying supernova continuum can be reasonably well approximated by a blackbody. The SED at bluer wavelengths is known to deviate from a blackbody approximation due to line blanketing from iron-group elements (P. H. Hauschildt & E. Baron 1995; E. Baron et al. 2003; L. Dessart & D. J. Hillier 2005; K. A. Bostroem et al. 2024). However, at longer wavelengths, emission from additional processes becomes important, rendering a single blackbody unable to capture the continuum behavior of the spectrum. These processes include: (1) the increasing fraction of free–free emission at longer wavelengths (D. K. Aitken et al. 1988a), (2) bluer flux redistributed to the IR by line scattering, (3) heated circumstellar dust located within the unshocked CSM (D. K. Aitken et al. 1988b; P. F. Roche et al. 1993; A. Sarangi et al. 2018), or some combination of the above (D. H. Wooden et al. 1993).

We performed a series of Monte Carlo (MC) fits utilizing a pair of two-component models. The first model is the sum of a blackbody modeling the peak of the emission and a free–free emission component that provided excess emission at longer wavelengths. The second model replaces the free–free emission with a second blackbody component. The errors on the fit parameters reported below include both the fit error and the errors derived from MC distributions added in quadrature. At the time of our observations (+33.6 days), the optical+NIR continuum of the combined spectrum is well fit by a blackbody

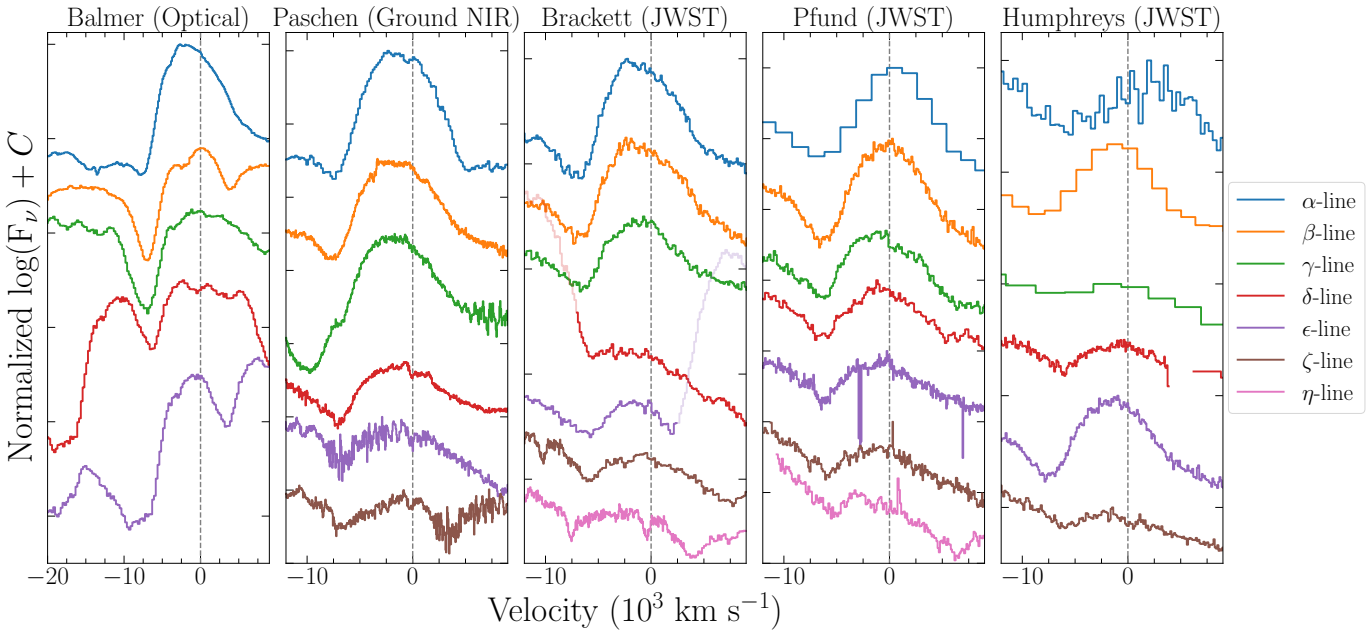

Figure 5. Hydrogen lines separated by series. Wavelengths of the individual transitions can be found in Section 3 and their measured velocities in Table 5. Strongly blended lines include: Paα with Brδ and Brϵ, Pfα with Huβ, Pfβ with Huϵ, and possibly Huγ with unknown lines.

with temperature $T_{\rm BB} = 6150 \pm 60$ K, broadly consistent with the $T_{\rm BB} = 5900 \pm 100$ K found by E. A. Zimmerman et al. (2024) derived from *UBVRI* photometry at $t = 34.06$ days. The addition of a free–free component ($T = 6100 \pm 1500$ K) accounts for the underprediction of the flux at $\lambda > 4$ μm; however an additional blackbody at $T_{\rm BB} = 960 \pm 30$ K does just as well, if not slightly better, statistically at reproducing the observed continuum flux. A Markov Chain MC analysis shows that the parameters of the free–free fit are, in fact, insensitive to the data. Interestingly, the SED of SN 2024ggi at ∼55 days is well fit by a single blackbody with $T_{\rm BB} = 5000 \pm 100$ K. E. Baron et al. (2025) were able to model the continuum and line emission from SN 2024ggi, redward of 1 μm with a full NLTE model using a simple power-law density structure. This model includes the physics associated with scattering, line transitions, and free–free emission in a self-consistent manner, where the multicomponent fits presented here are only sensitive to the flux of the pseudo-continuum.

The comparable fit quality of the free–free fit and a cold blackbody to reproduce the residual emission renders us unable to address whether contributions from a dust continuum are necessary to match the observed flux at IR wavelengths. Such a dust component has been inferred as early as 60 days in SN 1987A (D. H. Wooden et al. 1993) and at 87 days in the case of the Type IIn SN 2010jl (A. Sarangi et al. 2018), but is not seen in SN 2004et at 64 days (R. Kotak et al. 2009). S. D. Van Dyk et al. (2024a) fit the early (∼4 days) CSM emission of SN 2023ixf with the combination of a 26,600 K blackbody and a 1600 K blackbody, attributing the IR excess to either dust or CO emission.

However, most observations of SNe II at MIR wavelengths have focused on the nebular phases, leaving the early phases relatively unexplored (T. Szalai et al. 2019) in terms of both temporal coverage and the source of the IR emission (e.g., SN ejecta, free–free emission, or heated CSM dust). The lack of a large excess at longer IR wavelengths suggests that either any dust component is significantly dimmer than the supernova itself (the pre-explosion flux values of the progenitor and its surroundings were 30.5 ± 1.2 μJy and 22.1 ± 1.0 μJy, respectively, in the 3.6 μm and 4.5 μm Spitzer bands; S. D. Van Dyk et al. 2024b) or most of the nearby dust has been destroyed by the interaction and subsequent shocks. K. Medler et al. (2025a) find evidence for dust emission decreasing with time in SN 2023ixf, beginning at their earliest epoch ($t \sim 253$ days). The dust emission at 10 μm in their data is ∼5.6 mJy, whereas our fit gives a flux at this early time of only ∼2 mJy, making it unlikely that the excess flux is really due to emission from warm dust.

Additional plateau-phase data and full NLTE modeling, including free–free emission and other physical processes, are necessary to draw conclusions about the nature of any preexisting molecules or dust in SNe II, in order to accurately estimate the amount of newly formed dust at later epochs. Physically, there is a contribution to the MIR flux from free–free emission, and the underlying continuum is not actually that of a blackbody, even if the multicomponent fits are not statistically sensitive to it. Therefore, we reject the interpretation that the MIR excess is due to warm dust.

6. Line Velocities and Profiles

Figure 5 shows the strong, clearly identified hydrogen lines separated by series. In general, the widths of the line profiles are remarkably consistent across each individual series, except where the lines of the Brackett, Pfund, and Humphreys series blend and overlap. These widths are also consistent when compared according to the corresponding transition (e.g., alpha line, beta line, etc.) within each series. Individual lines of the Humphreys series are also subject to undersampling due to the lower resolution of the MIRI/LRS data relative to the NIRSpec data, particularly in the Huγ line. Weak and tentatively identified H lines in the MIRI data are excluded from the following analysis due to these issues.

Table 5
Hydrogen Absorption Velocities

Line	Rest Wavelength (μm)	Velocity (km s^{-1})	Error (km s^{-1})
Balmer series			
Hδ	0.4102	−6310	420
Hγ	0.4340	−6480	420
Hβ	0.4861	−6790	420
Hα	0.6563	−7630	420
Paschen series			
Paη	0.902	−6850	400
Paζ	0.923	−6870	400
Paϵ	0.955	−6940	400
Paδ	1.005	−6940	400
Paγ	1.094	−6860	400
Paβ	1.282	−7890	400
Paα	1.875	−7720	380
Brackett series			
Brγ	2.166	−6760	330
Brβ	2.625	−7170	270
Brα	4.051	−7470	290
Pfund series			
Pfζ	2.873	−6540	250
Pfϵ	3.039	−6520	230
Pfδ	3.297	−6700	360
Pfγ	3.741	−6830	320
Pfβ	4.654	−6750	260
Pfα	7.46	−7970	2980
Humphreys series			
Huζ	4.376	−6270	300
Huδ	5.129	−6520	240
Huα	12.372	−6760	1400

Note. The following H I lines are too blended or at too low a resolution to accurately measure: Brδ, Brϵ, Huβ, Huγ, Huϵ, Huη.

6.1. Hydrogen Velocities

To fit the absorption velocities, a hand-selected linear continuum is fit using nearby regions free of other lines. Where the lines show a defined P Cygni shape, this continuum is subtracted, and the continuum level used to separate the line into absorption and emission components. In lines without a clear P Cygni profile or which are contaminated by strong blending (such as the Hβ, Hγ, and Hδ lines), this continuum is fit "peak-to-peak," and the fitting procedure is identical to that of S. Davis et al. (2019) and M. Shahbandeh et al. (2022, 2024). Each measurement is repeated 500 times, where the flux is resampled from a normal distribution with its standard deviation equal to the flux error of each individual spectral point. The values are shown in Table 5, where the reported errors include both the fitting error and the resolution error of the spectrum added in quadrature. In most cases, the resolution error dominates over the fitting error.

Superior fits were achieved for several lines by including a secondary absorption component. In selected cases, (e.g., Hβ and Paγ) these secondary components could be attributed to blending by additional lines (Fe II λ4303 and He I λ1.083, respectively). However, in most cases, this second component was only added to better approximate the absorption component of the P Cygni profile, which is known to be non-Gaussian (J. Teffs et al. 2020; M. Shahbandeh et al. 2022). In these instances, the absorption minimum was obtained from the multicomponent fit, with the reported error determined in the same manner as in the single-Gaussian case, as the resolution error consistently dominates over the fit errors. We also fit the Fe II λ5169 line, as its velocity is commonly taken to represent of the photospheric velocity in SNe II. We find the absorption minimum to be -6120 ± 420 km s^{-1}.

From the results of these fits, we see that the absorption minima follow a near-monotonic trend, where the lower-energy transitions (e.g., alpha lines) have faster absorption minima than high-energy lines within their own series. For hydrogen lines with strong, unblended emission components (such as Hα and Brα), the emission peaks are blueshifted by $\sim$3000 km s^{-1}. Models of the emission lines in SNe II require steep density profiles (power laws with indices $n \lesssim -8$) in order to achieve this blueshift (M. Duschinger et al. 1995; L. Dessart & D. J. Hillier 2005). The observed properties of SN 2023ixf are consistent with the trends found by J. P. Anderson et al. (2014) that larger blueshifts are correlated with brighter V-band maxima and a greater decline rate during the plateau (s_2) in SNe II. From these observations, we therefore conclude that the ejecta of SN 2023ixf must also have a steep density profile.

6.2. IR Hydrogen Line Profiles

The line profiles of key transitions are known to encode important information about the ejecta, environment, and evolution of SNe II. Well-known examples of this structure include (but are not limited to): high-velocity absorptions arising from both the CDS and the forward/reverse shocks (N. N. Chugai et al. 2007; L. Dessart & D. J. Hillier 2022), the "Cachito" feature (C. P. Gutiérrez et al. 2017), the Bochum event in SN 1987A (i.e., a ^{56}Ni bullet, H. P. Larson et al. 1987; M. M. Phillips & S. R. Heathcote 1989; V. P. Utrobin et al. 1995), dust absorption (L. B. Lucy et al. 1989; N. Smith et al. 2008; C. Gall et al. 2014), and clumpy material (A. Singh et al. 2024). Here, we systematically examine several structures seen in the five named series producing strong hydrogen lines across the spectrum.

6.2.1. High-velocity Features

We first look for evidence of HV features (HVFs) in our time-series spectroscopic data shown in Figures 6 and 7. These features can form a multitude of profiles as demonstrated by N. N. Chugai et al. (2007). In their model including circumstellar interaction, HVFs can arise from ionization of the outer ejecta by the reverse shock. Further structure originating from absorption by the CDS and outward mixing of the CDS produce additional narrow and broad HVFs, respectively. These results have been verified in other NLTE models of SNe II (L. Dessart et al. 2013; L. Dessart & D. J. Hillier 2022). The "Cachito" is one manifestation of this complexity, where early, shallow Hα HVFs likely result from the reverse shock, while later, narrow HVFs are connected to the CDS and forward shock.

As seen in the left two panels of Figure 8, the absorption profile of Hα is complex in SN 2023ixf, showing both a shallow, broad HV component and the narrow, weak P Cygni

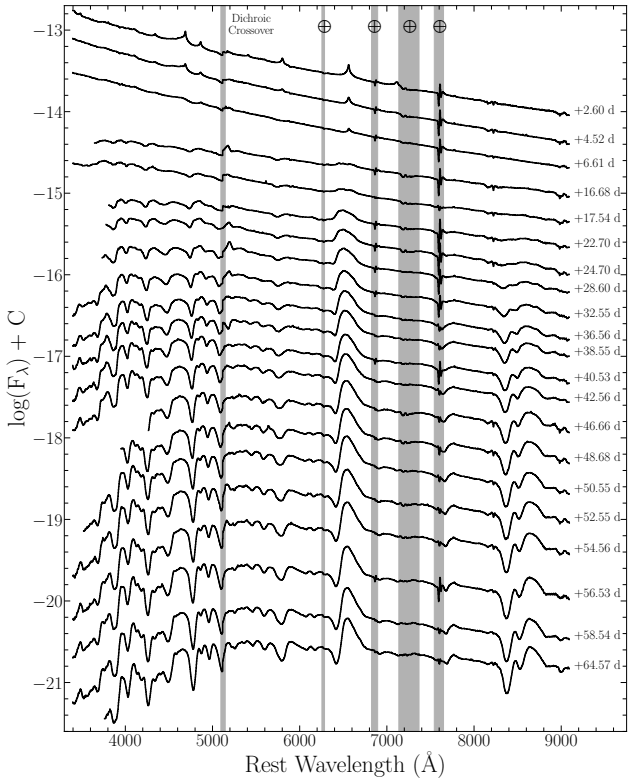

Figure 6. Ground-based time-series optical spectra obtained with UH88/SNIFS by the SCAT collaboration. Regions of strong telluric absorption and the dichroic crossover region at ∼5100 Å are marked in gray.
(The data used to create this figure are available in the online article.)

absorption. There is also strong contamination from the telluric O_2 γ-band at 6280 Å (−13,200 km s^{-1} relative to Hα). A "Cachito" originating from Si II λ6355 is ruled out, as the inferred velocity would be less than the photospheric velocity measured from the Fe II λ5169 line, consistent with other SN 2023ixf time-series analyzes (R. S. Teja et al. 2023; A. Singh et al. 2024). Time-series optical spectra of SN 2023ixf show that this HVF appears simultaneously with the P Cygni component (∼+16.7 days after explosion in our data), gradually weakening and slowing until around +47 days, when its evolution becomes difficult to separate from the telluric contamination at −13,200 km s^{-1}. The weakening and slowing of the HVF are consistent with the behavior expected from the combination of cooling via geometrical dilution and the propagation of the reverse shock to deeper layers.

N. N. Chugai et al. (2007) suggest that such HVFs may also be visible in both Hβ and the He I 1.083 μm lines, and such HVFs have been previously seen in SN 2017eaw (S. Tinyanont et al. 2019). We find no evidence for HVFs in either line in our data (but see A. Singh et al. 2024 for an alternative view), nor evidence for HVFs in additional IR hydrogen lines. In particular, the Hβ HVF is likely to be extremely weak due to the low Sobolev optical depth. For the majority of additional hydrogen lines covered by JWST, the estimated Sobolev optical depths (see Equations (4) and (13) of D. J. Jeffery & D. Branch 1990) will be weaker than that of Hβ, explaining the absence of HVFs in the IR H lines. Any weak HVFs that may be visible in strong NIR lines such as Paα are obscured by blending.

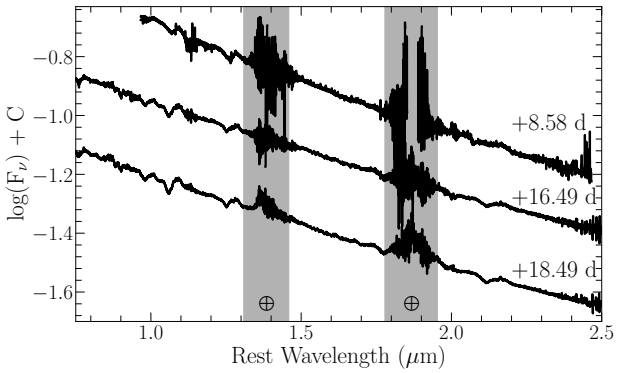

Figure 7. Ground-based NIR spectra obtained by HISS (K. Medler et al. 2025b) using Keck II/NIRES and IRTF/SpeX. Channel gaps arising from atmospheric absorptions are marked in gray.
(The data used to create this figure are available in the online article.)

6.2.2. Clumping in Paα?

A. Singh et al. (2024) note that between +9.9 and +25.8 days, additional intricate structures can be seen, appearing at similar velocities in both the Hα and Hβ emissions. They attribute these structures to multiple clumps in the interaction region. Consistent with their findings, by the time of our JWST observations, these structures are absent from the Hα and Hβ lines. However, small-scale structure is seen atop the Paα line from our JWST/NIRSpec observations, with the $v \approx 0$ km s^{-1} clump appearing in Paα with the same shape and velocity as first seen in Hα (see Figure 9). No other structures matching those seen previously in Hα are identified in either Paα or other strong hydrogen lines in our optical through MIR spectra. Nor can this structure be attributed to the nearby Brδ and Brϵ lines, whose profiles only blend at the edges of the Paα profile, as evidenced by the similarities between the Paα profile and those of Hα and other Paschen lines. Furthermore, no other weaker hydrogen lines exist at these wavelengths that originate from levels identified elsewhere in our spectra.

6.2.3. Additional Structure in IR Hydrogen Lines

As seen in Figure 8, multiple additional structures appear in different subsets of the IR hydrogen lines. These structures include: "flat-topped" emission profiles (such as those observed in the strong emissions of Paβ and Paγ), a blue emission notch (observed in Hα, Paβ, and Brβ), and a red emission shoulder (found in Paβ, Paγ, Paδ, and Pfγ). Such structures may arise independently through a variety of effects, but can also emerge in combination through a single mechanism in some instances (see, for example, the Bochum event). Among strong IR hydrogen lines deviating from the expected P Cygni profile, only Paβ shows all three structures. Below, we detail several possible origins of these additional structures and evaluate the consistency of these mechanisms with the known properties of SN 2023ixf.

"Flat-topped" emission lines are common to many types of stellar explosions and have been observed in multiple SNe II (A. Pastorello et al. 2009; C. Inserra et al. 2013; C. P. Gutiérrez et al. 2014, 2020; K. Medler et al. 2023). Also referred to as detached profiles (D. J. Jeffery & D. Branch 1990), these flat-tops arise from shells of material above the photosphere. During the photospheric phases, lines still show an absorption trough, in contrast to their box-like appearance during nebular phases.

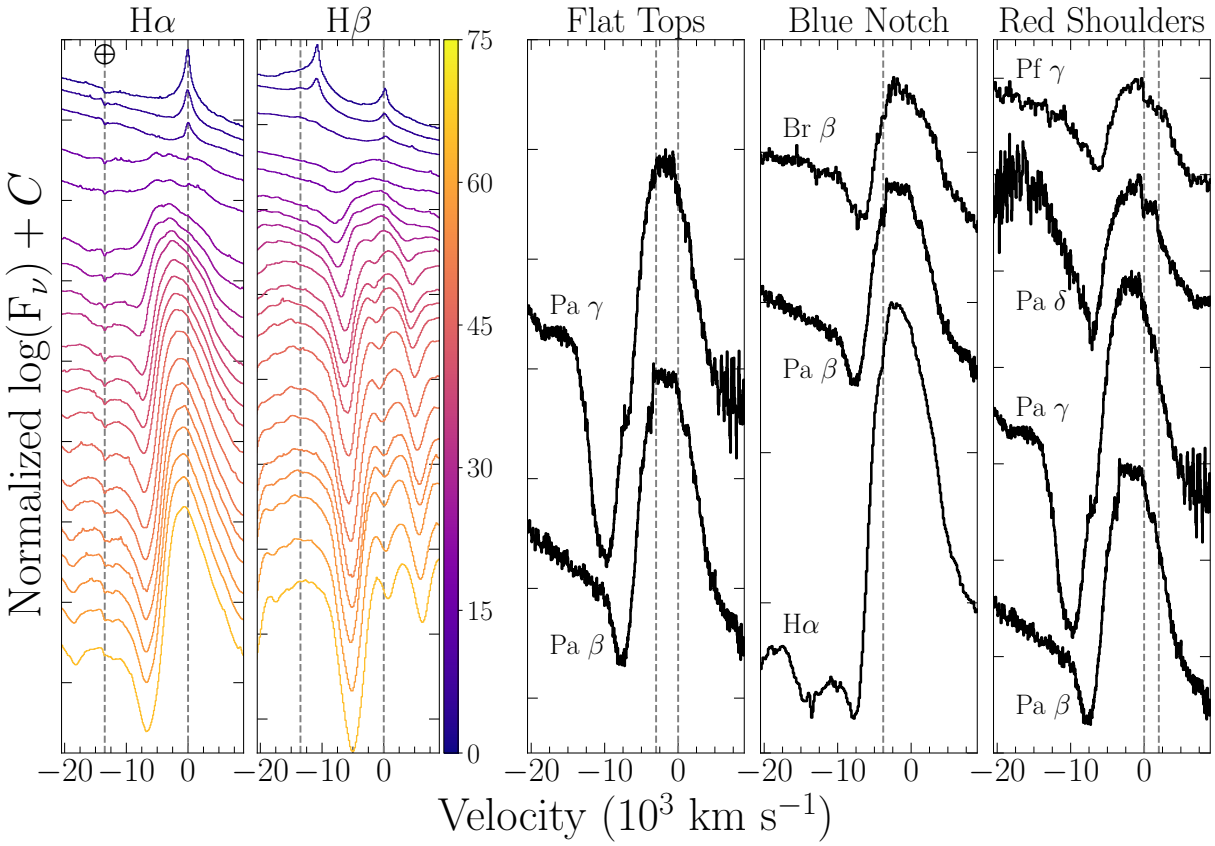

Figure 8. Left panels: SCAT time-series optical spectra of Hα and Hβ, colored by days from the explosion. In contrast to A. Singh et al. (2024), we find no evidence of an HVF in Hβ at $-13{,}500$ km s^{-1}. Right panels: examples of line structure seen in IR hydrogen lines at $\sim$33 days. Vertical gray lines denote the velocity extent of the structures. The "flat-tops" of lines extend from ~-3000 to 0 km s^{-1}, the blue notch is centered at ≈-3800 km s^{-1}, and the red shoulders extend from $\sim$0 to 2000 km s^{-1}, consistent across all lines showing each structure within the resolution errors.

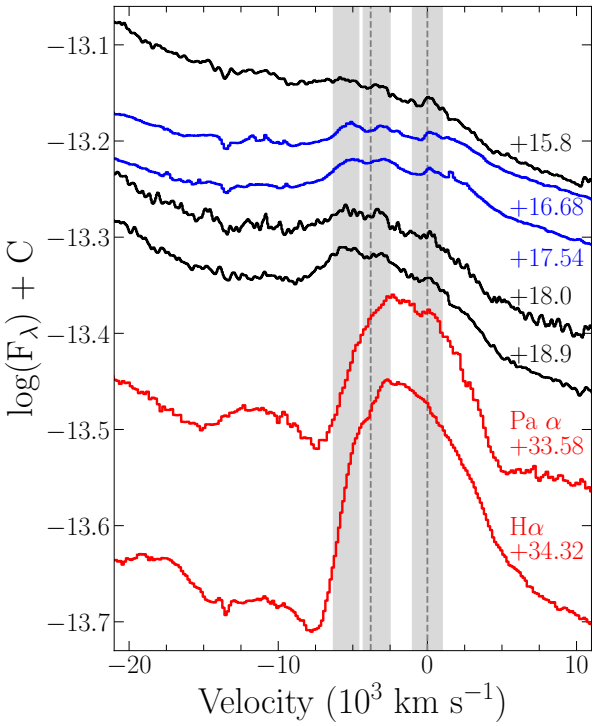

Figure 9. Clumpy structure in Hα from A. Singh et al. (2024; black) and SCAT (blue) compared to the Hα and Paα profiles (red) from our near-contemporaneous SED of SN 2023ixf. Only the structure arising from the clump at $v = 0$ km s^{-1} is seen atop Paα. All other clumps seen previously in Hα are no longer present.

However, in SN 2023ixf, the edges of the flat-tops extend from ~-3000 to 0 km s^{-1}, well below the inferred photospheric velocity of 6120 km s^{-1}. Emission from the CDS could also produce a flat-topped profile, as suggested by A. Pastorello et al. (2009) in the case of SN 1999ga. However, as the CDS forms above the photosphere, the emission would appear at superphotospheric velocities, not the subphotospheric velocities seen in SN 2023ixf. This is confirmed by the models of K. A. Bostroem et al. (2024), which show such a red shelf appearing at $\sim$9200 km s^{-1} in Hα around 50 days after explosion. C. Inserra et al. (2013) attribute the "flat-topped" lines they see during the photospheric phases of SNe 1995ad and 1996W to underlying H II regions. We can, however, rule out this possibility because extensive pre-explosion imaging reveals SN 2023ixf to be separated by $\sim1''$ from NGC 5461, the nearest observed H II region in M101 (J. L. Pledger & M. M. Shara 2023; S. D. Van Dyk et al. 2024b).

Instead, we suggest that these flat-topped profiles likely arise from a combination of geometric and opacity effects. The inferred steep density profile from velocity measurements effectively creates a region with a small, nonzero constant opacity, resulting in the flat-topped profiles, which are a special case of the detached profiles outlined by D. J. Jeffery & D. Branch (1990). Such flat-topped profiles are not seen in weaker lines originating from higher-level transitions, because they have effectively no opacity at the photosphere and therefore appear as the pure absorption lines described by E. Baron et al. (2025) as their "detached lines" case in SN 2024ggi. The stronger H lines (e.g., Hα, Paα, Brα) involve the only levels sufficiently populated across the steep density slope

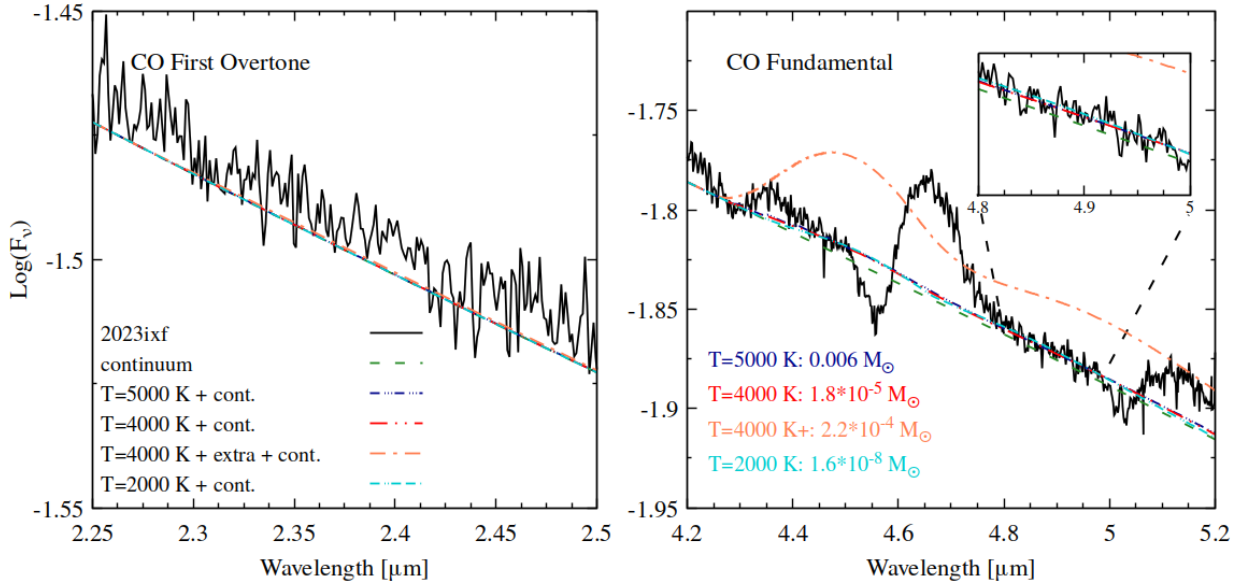

Figure 10. Temperature-dependent limits on CO emission in SN 2023ixf. Note that the P Cygni profiles at ∼4.2–4.3, 4.5–4.8, and 5–5.2 μm are from Huζ, Pfβ + Huϵ, and Huδ, respectively. The representative examples of the emission from various combinations of temperature and mass in the optically thin case are shown for the first overtone band (left) and the fundamental band (right). The maximum CO mass is determined based on the fundamental band, and varies between 1.6×10^{-8} and 0.006 $M_{\odot}$ with temperature. The orange dashed–dotted 4000 K signal demonstrates a realistic detection of the CO fundamental, including an extra continuum (above that of a blackbody) to mimic effects of free–free emission and lines. The inset shows the nondetections compared to the continuum in a region of the fundamental free of H lines.

to have a varying opacity over the narrow velocity range and produce the typical P Cygni emission peak.

Several IR lines show depressed flux in the red half of their emission peaks starting at zero velocity, with a corresponding shoulder at ∼2000 km s^{-1}. This is most prominently seen as an abrupt drop in flux in the Paschen series lines, but also as steeply sloped decreases in flux in the strong Brackett and Pfund lines (at lower S/N). At late times, one potential origin of such a depression is obscuration by newly formed dust in the SN ejecta (L. B. Lucy et al. 1989; A. Bevan et al. 2019). While our SED modeling in Section 5 cannot conclusively address the potential presence of dust, our combined analysis suggests the ejecta is too hot to form either molecules (see Section 5 and Section 7) or new dust, consistent with previous studies of other SNe II with early IR excesses (D. H. Wooden et al. 1993; A. Sarangi et al. 2018). Therefore, we consider it highly unlikely that this red shoulder originates from newly formed dust in the ejecta. Preexisting heated dust, such as that found by K. Medler et al. (2025a), is unable to produce this obscuration as it is located exterior to the ejecta.

An additional notch is also seen on the blue side of the Hα emission peak at ∼−3800 km s^{-1}. This notch is visible in the time series of spectra of A. Singh et al. (2024) until ∼32 days after explosion (see their Figure 6), consistent with the optical time series presented in Figure 6. When combined with the red shoulder observed in several other hydrogen lines, the combined structure is reminiscent of the Bochum event observed in SN 1987A (M. M. Phillips & S. R. Heathcote 1989; R. W. Hanuschik & G. J. Thimm 1990). During the Bochum event, NIR profiles of the hydrogen lines showed a significant asymmetric, double-peaked profile (see, for example, Figure 1 of H. P. Larson et al. 1987), with the two peaks of the Paα line separated by ∼4000 km s^{-1}. No such double-peaked profiles are seen in SN 2023ixf, seemingly ruling out the presence of an Ni bullet.

The velocity of the blue notch does, however, correspond to the minima between the two higher-velocity clumps identified by A. Singh et al. (2024). In their scenario, the clumps in the CSM are fully overrun by the SN ejecta between 30 and 40 days, and the smooth nature of the P Cygni profile emerges in later epochs. However, the lack of strong, uncontaminated lines in the ground-based IR data and the sparsity of temporal coverage relative to optical wavelengths provide no strong evidence for the existence of the clumps seen in the IR (see S. H. Park et al. 2025 for discussions of small-scale line structure in ground-based NIR spectra of SN 2023ixf).

As highlighted by D. J. Jeffery & D. Branch (1990), density peaks are far more likely to occur than detached atmospheres within the supernova ejecta. Such density peaks can create profiles that are qualitatively similar to those seen in SN 2023ixf (see their Figure 7), albeit with a secondary blue emission maximum due to the opacity jump from the density peak. However, when the opacity difference is small (as is expected if turbulent mixing occurs within the ejecta), these variations in the line profile may not be easily identifiable due to the density peaks being smoothed out (D. J. Jeffery & D. Branch 1990). However, the models they present place the density peak above the photosphere, while these structures in SN 2023ixf lie below the inferred photospheric velocity. Such density peaks may be present in SN 2023ixf, possibly due to the existence of a dusty torus as inferred from polarimetric observations (S. S. Vasylyev et al. 2023; A. Singh et al. 2024). But it is important to note that one-dimensional, spherically symmetric codes such as `SYNOW` cannot fully capture the inherently multidimensional structure of the ejecta. Future detailed multidimensional radiation-hydrodynamic modeling of the asymmetric structures, any associated shocks, and viewing angle dependences present in SN 2023ixf may distinguish between these possible scenarios.

7. Limits on Carbon Monoxide

The spectrum of SN 2023ixf shows no evidence for the formation of molecules (e.g., CO or SiO). As seen in Section 5 the excess continuum is well fit by just a ∼1000 K Planck function at wavelengths >4 μm and by a ∼6000 K Planck function at shorter wavelengths. Therefore we obtain upper limits on the amount of preexisting molecules and dust, which sets a baseline for observations at later times. The in-depth procedure by which we place these upper limits for the plateau phase of SNe IIP is detailed by M. Shahbandeh et al. (2024). We briefly summarize it here for clarity, and refer interested readers to that paper and references therein for further details.

To obtain upper limits on CO in SN 2023ixf during the plateau phase, we assumed an isothermal ejecta with a density structure typical for an SN IIP. The density gradient was obtained as done by M. Shahbandeh et al. (2024) and gives a power-law index of $n \approx -2.5$. Figure 10 shows the CO emission for both the fundamental (right) and first overtone (left) of CO, and their flux for given temperatures in comparison with observation. The opacity peaks at approximately 2500–3000 K and decreases by roughly six orders of magnitude at the recombination temperature of H. Because the opacity and the specific emissivity relative to the continuum flux in the first CO overtone are smaller than those for the fundamental band by a factor of the order of ≈100, the fundamental band provides the upper limits, illustrating the importance of JWST data. If CO exists in the CSM it would add opacity due to cold CO in the surroundings of SN 2023ixf. Since no CO is observed, any preexisting CO is optically thin. The emission will be $\propto T$ in the fundamental band. If CO is observed in SN 2023ixf at later epochs, it will be due to molecules synthesized in the ejecta and not due to existing molecules in the CSM, which will not evolve in time. Our simple exercise does not constrain anything about the CO, because there is, in fact, no evidence in the data for the presence of CO at this epoch. S. H. Park et al. (2025) find about $2 \times 10^{-4}\ M_{\odot}$ of CO with $T \approx 3000$ K in SN 2023ixf at +199 days from ground-based spectra.

8. Conclusion

Here, we present observations of SN 2023ixf with JWST taken 33.6 days after explosion, which roughly corresponds to the midpoint of the plateau phase. The NIR+MIR spectra are dominated by H lines, while contemporaneous ground-based observations in the optical and NIR reveal spectra consistent with other SNe II at the observed epoch. The comparisons of JWST NIR spectra to SN 2022acko show that the correlations between H line widths and velocities and V-band peak magnitude continue into the IR. Comparisons of MIR spectra to SNe 1987A and 2022acko at similar evolutionary phases reveal that only the strongest lines such as the Pfα + Huβ blend and Huα lines are prominent at low spectral resolutions.

Fits to the panchromatic (0.35–14 μm) SED reveal that the spectral continuum can be fit to a blackbody with $T_{\rm BB} = 6150 \pm 60$ K, with a small excess at $\lambda \gtrsim 4$ μm. This excess can be fit by the inclusion of free–free emission or by adding a second blackbody component. We reject the explanation that the excess emission is caused by warm dust, based on the physical processes occurring in the SN ejecta and the time evolution of the MIR flux. The nature of and need for additional emission components vary across the small number of SNe II with early MIR observations. Caution should be given to inferring dust excess during the plateau from single-epoch spectroscopy.

Furthermore, no observational signals of molecules (e.g., CO) are detected; and we place limits on the mass of preexisting CO in the ejecta. Such measures are necessary to ensure the amount of newly synthesized molecules and dust can be accurately traced over time. This is of critical importance for SNe II that are assumed to arise from dusty RSG progenitors such as SN 2023ixf, where such signals may also arise from heated CSM, as suggested by later observations (K. Medler et al. 2025a).

These observations will form the basis of what is expected to be decades of follow-up of SN 2023ixf using JWST. Paper II of this series (K. Medler et al. 2025a) explores the panchromatic spectral evolution of the nebular phase with JWST observations (C. Ashall et al. 2023b, 2024), and future papers will focus on the evolution of molecules and dust in SN 2023ixf. These and other future observations will provide the opportunity to trace potential molecule formation and dust growth in what is likely to be one of the closest SNe II in the JWST era, and will provide valuable insight into the formation and origin of dust in the early Universe.

Acknowledgments

We thank Alison Vick, Stephan Birkmann, George Chapman, Amanda Marrione, Brian McLean, Ed Nelan, Alberto Noriega-Crespo, Beverly Owens, Scott Stallcup, and the entire JWST operations and scheduling teams for their hard work in scheduling and executing these time-critical observations.

J.D., C.A., K.M., P.H., E.B., T.M., and M.S. are supported in part by NASA grants JWST-GO-02114, JWST-GO-02122, JWST-GO-03726, JWST-DD-04436, JWST-DD-04522, JWST-GO-4217, JWST-DD-04575, JWST-GO-5057, JWST-GO-5290, JWST-GO-6023, and JWST-GO-6677. J.D., C.A., and E.B. were supported in part by HST-AR-17555, Support for program Nos. 2114, 2122, 3726, 4436, 4522, 4575, 5057, 5290, 6023, 6677, and 17555 was provided by NASA through grants from the Space Telescope Science Institute, which is operated by the Association of Universities for Research in Astronomy, Inc., under NASA contract NAS 5-03127. P.H. is supported in parts by the NSF grant AST-230639. L.G. acknowledges financial support from AGAUR, CSIC, MCIN and AEI 10.13039/501100011033 under projects PID2023-151307NB-I00, PIE 20215AT016, CEX2020-001058-M, ILINK23001, COOPB2304, and 2021-SGR-01270. M.D.S. is funded by the Independent Research Fund Denmark (IRFD, grant No. 10.46540/2032-00022B) and by an Aarhus University Research Foundation Nova project (AUFF-E-2023-9-28). J.T.H. was supported by NASA grant 80NSSC23K1431. S.M. is funded by Leverhulme Trust grant RPG-2023-240.

This work is based on observations made with the NASA/ESA/CSA James Webb Space Telescope. The data were obtained from the Mikulski Archive for Space Telescopes at the Space Telescope Science Institute, which is operated by the Association of Universities for Research in Astronomy, Inc., under NASA contract NAS 5-03127 for JWST. These observations are associated with program No. 4522. The specific observations analyzed in this work can be accessed via DOI: 10.17909/ekjp-5b33.

This work was supported by a NASA Keck PI Data Award, administered by the NASA Exoplanet Science Institute. Data presented herein were obtained at the W. M. Keck Observatory

from telescope time allocated to the National Aeronautics and Space Administration through the agency's scientific partnership with the California Institute of Technology and the University of California. The Observatory was made possible by the generous financial support of the W. M. Keck Foundation. The authors wish to recognize and acknowledge the very significant cultural role and reverence that the summit of Maunakea has always had within the indigenous Hawaiian community. We are most fortunate to have the opportunity to conduct observations from this mountain.

Based on observations made with the Nordic Optical Telescope, owned in collaboration by the University of Turku and Aarhus University, and operated jointly by Aarhus University, the University of Turku and the University of Oslo, representing Denmark, Finland and Norway, the University of Iceland and Stockholm University at the Observatorio del Roque de los Muchachos, La Palma, Spain, of the Instituto de Astrofisica de Canarias. The NOT data were obtained under program ID P66-506.

Facilities: JWST (NIRSpec and MIRI), NOT (ALFOSC), Keck:II (NIRES), IRTF (Spex), UH2.2m (SNIFS).

Software: JWST Science Calibration Pipeline (version 1.18.0; H. Bushouse et al. 2025), `spextractor` (A. Burrow et al. 2020), Astropy (Astropy Collaboration et al. 2013, 2018, 2022), NumPy (C. R. Harris et al. 2020), SciPy (P. Virtanen et al. 2020), Matplotlib (J. D. Hunter 2007), `dust-extinction` (K. Gordon 2023; K. D. Gordon et al. 2023).

ORCID iDs

J. M. DerKacy https://orcid.org/0000-0002-7566-6080
C. Ashall https://orcid.org/0000-0002-5221-7557
E. Baron https://orcid.org/0000-0001-5393-1608
K. Medler https://orcid.org/0000-0001-7186-105X
T. Mera https://orcid.org/0000-0001-5888-2542
P. Hoeflich https://orcid.org/0000-0002-4338-6586
M. Shahbandeh https://orcid.org/0000-0002-9301-5302
C. R. Burns https://orcid.org/0000-0003-4625-6629
M. D. Stritzinger https://orcid.org/0000-0002-5571-1833
M. A. Tucker https://orcid.org/0000-0002-2471-8442
B. J. Shappee https://orcid.org/0000-0003-4631-1149
K. Auchettl https://orcid.org/0000-0002-4449-9152
C. R. Angus https://orcid.org/0000-0002-4269-7999
D. D. Desai https://orcid.org/0000-0002-2164-859X
A. Do https://orcid.org/0000-0003-3429-7845
J. T. Hinkle https://orcid.org/0000-0001-9668-2920
W. B. Hoogendam https://orcid.org/0000-0003-3953-9532
M. E. Huber https://orcid.org/0000-0003-1059-9603
A. V. Payne https://orcid.org/0000-0003-3490-3243
D. O. Jones https://orcid.org/0000-0002-6230-0151
J. Shi https://orcid.org/0009-0008-3724-1824
M. Y. Kong https://orcid.org/0009-0005-5121-2884
S. Romagnoli https://orcid.org/0009-0003-8153-9576
A. Syncatto https://orcid.org/0009-0000-6821-9285
S. Moran https://orcid.org/0000-0001-5221-0243
E. Fereidouni https://orcid.org/0009-0001-9148-8421
P. J. Brown https://orcid.org/0000-0001-6272-5507
M. Engesser https://orcid.org/0000-0003-0209-674X
O. D. Fox https://orcid.org/0000-0003-2238-1572
L. Galbany https://orcid.org/0000-0002-1296-6887
E. Y. Hsiao https://orcid.org/0000-0003-1039-2928
T. de Jaeger https://orcid.org/0000-0001-6069-1139
S. Kumar https://orcid.org/0000-0001-8367-7591
J. Lu https://orcid.org/0000-0002-3900-1452
M. Matsuura https://orcid.org/0000-0002-5529-5593
P. A. Mazzali https://orcid.org/0000-0001-6876-8284
N. Morrell https://orcid.org/0000-0003-2535-3091
C. M. Pfeffer https://orcid.org/0000-0002-7305-8321
M. M. Phillips https://orcid.org/0000-0003-2734-0796
A. Rest https://orcid.org/0000-0002-4410-5387
S. Shiber https://orcid.org/0000-0001-6107-0887
L. Strolger https://orcid.org/0000-0002-7756-4440
N. B. Suntzeff https://orcid.org/0000-0002-8102-181X
T. Temim https://orcid.org/0000-0001-7380-3144
S. Tinyanont https://orcid.org/0000-0002-1481-4676
Q. Wang https://orcid.org/0000-0001-5233-6989
R. Wesson https://orcid.org/0000-0002-4000-4394
S. H. Park https://orcid.org/0000-0001-7488-4337
J. Rho https://orcid.org/0000-0003-3643-839X

References

Abac, A. G., Abbott, R., Abouelfettouh, I., et al. 2025, ApJ, 985, 183
Aitken, D. K., Smith, C. H., James, S. D., et al. 1988a, MNRAS, 231, 7P
Aitken, D. K., Smith, C. H., James, S. D., et al. 1988b, MNRAS, 235, 19P
Anderson, J. P., Dessart, L., Gutierrez, C. P., et al. 2014, MNRAS, 441, 671
Ashall, C., Baron, E., DerKacy, J. M., et al. 2023a, JWST Proposal. Cycle 1, ID. #4522,
Ashall, C., Baron, E., DerKacy, J. M., et al. 2023b, JWST Proposal. Cycle 2, ID. #4575,
Ashall, C., Hoeflich, P. A., Shahbandeh, M., et al. 2024, JWST Proposal. Cycle 3, ID. #5290,
Astropy Collaboration, Price-Whelan, A. M., Lim, P. L., et al. 2022, ApJ, 935, 167
Astropy Collaboration, Price-Whelan, A. M., Sipőcz, B. M., et al. 2018, AJ, 156, 123
Astropy Collaboration, Robitaille, T. P., Tollerud, E. J., et al. 2013, A&A, 558, A33
Barlow, M. J. 1978a, MNRAS, 183, 367
Barlow, M. J. 1978b, MNRAS, 183, 397
Barlow, M. J. 1978c, MNRAS, 183, 417
Baron, E., Ashall, C.,, DerKacy, J. M., et al. 2025, ApJ, 994, 249
Baron, E., Nugent, P. E., Branch, D., et al. 2003, ApJ, 586, 1199
Berger, E., Keating, G. K., Margutti, R., et al. 2023, ApJL, 951, L31
Bersten, M. C., Orellana, M., Folatelli, G., et al. 2024, A&A, 681, L18
Bertoldi, F., Cox, P., Neri, R., et al. 2003, A&A, 409, L47
Bevan, A., Wesson, R., Barlow, M. J., et al. 2019, MNRAS, 485, 5192
Böker, T., Beck, T. L., Birkmann, S. M., et al. 2023, PASP, 135, 038001
Bostroem, K. A., Pearson, J., Shrestha, M., et al. 2023, ApJL, 956, L5
Bostroem, K. A., Sand, D. J., Dessart, L., et al. 2024, ApJL, 973, L47
Brooker, E. S., Stangl, S. M., Mauney, C. M., & Fryer, C. L. 2022, ApJ, 931, 85
Burrow, A., Baron, E., Ashall, C., et al. 2020, ApJ, 901, 154
Bushouse, H., Eisenhamer, J., Dencheva, N., et al. 2025, JWST Calibration Pipeline, v1.18.0, Zenodo
Catchpole, R. M., Whitelock, P. A., Feast, M. W., et al. 1988, MNRAS, 231, 75P
Cernuschi, F., Marsicano, F., & Codina, S. 1967, AnAp, 30, 1039
Chandra, P., Chevalier, R. A., Maeda, K., Ray, A. K., & Nayana, A. J. 2024, ApJL, 963, L4
Chugai, N. N., Chevalier, R. A., & Utrobin, V. P. 2007, ApJ, 662, 1136
Davis, S., Hsiao, E. Y., Ashall, C., et al. 2019, ApJ, 887, 4
de Jaeger, T., Galbany, L., González-Gaitán, S., et al. 2020, MNRAS, 495, 4860
de Vaucouleurs, G., de Vaucouleurs, A., Corwin, H. G., Jr., et al. 1991, Third Reference Catalogue of Bright Galaxies (Springer)
Dell'Agli, F., Ventura, P., Schneider, R., et al. 2015, MNRAS, 447, 2992
Dessart, L. 2025, Astronomy & Astrophysics, 703, A287
Dessart, L., & Hillier, D. J. 2005, A&A, 437, 667
Dessart, L., & Hillier, D. J. 2022, A&A, 660, L9
Dessart, L., Hillier, D. J., Waldman, R., & Livne, E. 2013, MNRAS, 433, 1745
Di Criscienzo, M., Dell'Agli, F., Ventura, P., et al. 2013, MNRAS, 433, 313
Dong, Y., Sand, D. J., Valenti, S., et al. 2023, ApJ, 957, 28

Duschinger, M., Puls, J., Branch, D., Hoeflich, P., & Gabler, A. 1995, A&A, 297, 802
Dwek, E. 1998, ApJ, 501, 643
Dwek, E., Galliano, F., & Jones, A. P. 2007, ApJ, 662, 927
Dwek, E., Sarangi, A., & Arendt, R. G. 2019, ApJL, 871, L33
Ferrarotti, A. S., & Gail, H. P. 2006, A&A, 447, 553
Flinner, N., Tucker, M. A., Beacom, J. F., & Shappee, B. J. 2023, RNAAS, 7, 174
Fox, O. D., Chevalier, R. A., Dwek, E., et al. 2010, ApJ, 725, 1768
Fox, O. D., Chevalier, R. A., Skrutskie, M. F., et al. 2011, ApJ, 741, 7
Gall, C., Hjorth, J., & Andersen, A. C. 2011, A&ARv, 19, 43
Gall, C., Hjorth, J., Watson, D., et al. 2014, Natur, 511, 326
Gerardy, C. L., Fesen, R. A., Höflich, P., & Wheeler, J. C. 2000, AJ, 119, 2968
Gordon, K. 2023, karllark/dust_extinction: OneRelationForAllWaves, v1.2, Zenodo
Gordon, K. D., Clayton, G. C., Decleir, M., et al. 2023, ApJ, 950, 86
Grefenstette, B. W., Brightman, M., Earnshaw, H. P., Harrison, F. A., & Margutti, R. 2023, ApJL, 952, L3
Guetta, D., Langella, A., Gagliardini, S., & Valle, M. D. 2023, ApJL, 955, L9
Gutiérrez, C. P., Anderson, J. P., Hamuy, M., et al. 2014, ApJL, 786, L15
Gutiérrez, C. P., Anderson, J. P., Hamuy, M., et al. 2017, ApJ, 850, 89
Gutiérrez, C. P., Pastorello, A., Jerkstrand, A., et al. 2020, MNRAS, 499, 974
Hamuy, M., & Pinto, P. A. 2002, ApJL, 566, L63
Hanuschik, R. W., & Thimm, G. J. 1990, A&A, 231, 77
Harkness, R. P., Wheeler, J. C., Margon, B., et al. 1987, ApJ, 317, 355
Harris, C. R., Millman, K. J., van der Walt, S. J., et al. 2020, Natur, 585, 357
Hauschildt, P. H., & Baron, E. 1995, JQSRT, 54, 987
Hiramatsu, D., Tsuna, D., Berger, E., et al. 2023, ApJL, 955, L8
Hosseinzadeh, G., Farah, J., Shrestha, M., et al. 2023, ApJL, 953, L16
Hoyle, F., & Wickramasinghe, N. C. 1970, Natur, 226, 62
Hu, M., Wang, L., & Wang, X. 2025, ApJ, 984, 44
Hunter, J. D. 2007, CSE, 9, 90
Inserra, C., Pastorello, A., Turatto, M., et al. 2013, A&A, 555, A142
Itagaki, K. 2023, TNSTR, 1, 1158
Iwata, Y., Akimoto, M., Matsuoka, T., et al. 2025, ApJ, 978, 138
Jacobson-Galán, W. V., Dessart, L., Margutti, R., et al. 2023, ApJL, 954, L42
Jakobsen, P., Ferruit, P., Alves de Oliveira, C., et al. 2022, A&A, 661, A80
Jeffery, D. J., & Branch, D. 1990, in Supernovae, Jerusalem Winter School for Theoretical Physics, 6, ed. J. C. Wheeler, T. Piran, & S. Weinberg (Singapore: World Scientific)
Jencson, J. E., Pearson, J., Beasor, E. R., et al. 2023, ApJL, 952, L30
Jones, A. P. 2004, ASPC, 309, 347
Jones, A. P., Tielens, A. G. G. M., & Hollenbach, D. J. 1996, ApJ, 469, 740
Jones, O. C., Kavanagh, P. J., Barlow, M. J., et al. 2023, ApJ, 958, 95
Kendrew, S., Scheithauer, S., Bouchet, P., et al. 2015, PASP, 127, 623
Kheirandish, A., & Murase, K. 2023, ApJL, 956, L8
Kilpatrick, C. D., Foley, R. J., Jacobson-Galán, W. V., et al. 2023, ApJL, 952, L23
Kotak, R., Meikle, P., Pozzo, M., et al. 2006, ApJL, 651, L117
Kotak, R., Meikle, P., van Dyk, S. D., Höflich, P. A., & Mattila, S. 2005, ApJL, 628, L123
Kotak, R., Meikle, W. P. S., Farrah, D., et al. 2009, ApJ, 704, 306
Lantz, B., Aldering, G., Antilogus, P., et al. 2004, SPIE, 5249, 146
Larson, H. P., Drapatz, S., Mumma, M. J., & Weaver, H. A. 1987, European Southern Observatory Conf. and Workshop Proc. 26,
Larsson, J., Fransson, C., Sargent, B., et al. 2023, ApJL, 949, L27
Li, G., Hu, M., Li, W., et al. 2024, Natur, 627, 754
Li, Q., Wang, R., Fan, X., et al. 2020, ApJ, 900, 12
Liu, C., Chen, X., Er, X., et al. 2023, ApJL, 958, L37
Lucy, L. B. 1991, ApJ, 383, 308
Lucy, L. B., Danziger, I. J., Gouiffes, C., & Bouchet, P. 1989, in IAU Colloq. 120: Structure and Dynamics of the Interstellar Medium, 350, ed. G. Tenorio-Tagle, M. Moles, & J. Melnick (Springer)
Maiolino, R., Schneider, R., Oliva, E., et al. 2004, Natur, 431, 533
Mao, Y., Zhang, M., Cai, G., et al. 2023, TNSAN, 130, 1
Martinez, L., Bersten, M. C., Folatelli, G., Orellana, M., & Ertini, K. 2024, A&A, 683, A154
Matsuura, M., De Buizer, J. M., Arendt, R. G., et al. 2019, MNRAS, 482, 1715
Mazzali, P. A., Lucy, L. B., & Butler, K. 1992, A&A, 258, 399
Medler, K., Ashall, C., Hoeflich, P., et al. 2025a, ApJ, 993, 191
Medler, K., Ashall, C., Shahbandeh, M., et al. 2025b, ApJS, 281, 28
Medler, K., Mazzali, P. A., Ashall, C., et al. 2023, MNRAS, 518, L40
Meikle, W. P. S., Allen, D. A., Spyromilio, J., & Varani, G. F. 1989, MNRAS, 238, 193
Meikle, W. P. S., Kotak, R., Farrah, D., et al. 2011, ApJ, 732, 109
Michel, P. D., Mazzali, P. A., Perley, D. A., Hinds, K. R., & Wise, J. L. 2025, MNRAS, 539, 633
Miller, A. A., Smith, N., Li, W., et al. 2010, AJ, 139, 2218
Moriya, T. J., & Singh, A. 2024, PASJ, 76, 1050
Müller, B., Heger, A., Liptai, D., & Cameron, J. B. 2016, MNRAS, 460, 742
Nayana, A. J., Margutti, R., Wiston, E., et al. 2025, ApJ, 985, 51
Neustadt, J. M. M., Kochanek, C. S., & Smith, M. R. 2024, MNRAS, 527, 5366
Niu, Z., Sun, N.-C., Maund, J. R., et al. 2023, ApJL, 955, L15
Panjkov, S., Auchettl, K., Shappee, B. J., et al. 2024, PASA, 41, e059
Park, S. H., Rho, J., Yoon, S.-C., et al. 2025, A&A, 703, A227
Pastorello, A., Crockett, R. M., Martin, R., et al. 2009, A&A, 500, 1013
Perley, D., & Gal-Yam, A. 2023, TNSCR, 1, 1164
Phillips, M. M., & Heathcote, S. R. 1989, PASP, 101, 137
Pledger, J. L., & Shara, M. M. 2023, ApJL, 953, L14
Pozzo, M., Meikle, W. P. S., Fassia, A., et al. 2004, MNRAS, 352, 457
Qin, Y.-J., Zhang, K., Bloom, J., et al. 2024, MNRAS, 534, 271
Rank, D. M., Bregman, J., Witteborn, F. C., et al. 1988, ApJL, 325, L1
Ransome, C. L., Villar, V. A., Tartaglia, A., et al. 2024, ApJ, 965, 93
Ravensburg, E., Carenza, P., Eckner, C., & Goobar, A. 2024, PhRvD, 109, 023018
Rho, J., Geballe, T. R., Banerjee, D. P. K., et al. 2018, ApJL, 864, L20
Riess, A. G., Yuan, W., Macri, L. M., et al. 2022, ApJL, 934, L7
Roche, P. F., Aitken, D. K., & Smith, C. H. 1993, MNRAS, 261, 522
Sarangi, A., & Cherchneff, I. 2013, ApJ, 776, 107
Sarangi, A., Dwek, E., & Arendt, R. G. 2018, ApJ, 859, 66
Sarmah, P. 2024, JCAP, 2024, 083
Schlafly, E. F., & Finkbeiner, D. P. 2011, ApJ, 737, 103
Serrano-Hernández, D. B., Martínez-González, S., Jiménez, S., Silich, S., & Wünsch, R. 2025, A&A, 695, A271
Shahbandeh, M., Ashall, C., Hoeflich, P., et al. 2024, arXiv:2401.14474
Shahbandeh, M., Fox, O. D., Temim, T., et al. 2025, ApJ, 985, 262
Shahbandeh, M., Hsiao, E. Y., Ashall, C., et al. 2022, ApJ, 925, 175
Shahbandeh, M., Sarangi, A., Temim, T., et al. 2023, MNRAS, 523, 6048
Singh, A., Teja, R. S., Moriya, T. J., et al. 2024, ApJ, 975, 132
Slavin, J. D., Dwek, E., & Jones, A. P. 2015, ApJ, 803, 7
Slavin, J. D., Dwek, E., Mac Low, M.-M., & Hill, A. S. 2020, ApJ, 902, 135
Smartt, S. J. 2015, PASA, 32, e016
Smith, N., Foley, R. J., Bloom, J. S., et al. 2008, ApJ, 686, 485
Smith, N., Pearson, J., Sand, D. J., et al. 2023, ApJ, 956, 46
Smith, N., Silverman, J. M., Chornock, R., et al. 2009, ApJ, 695, 1334
Soker, N. 2023, RAA, 23, 081002
Soraisam, M. D., Szalai, T., Van Dyk, S. D., et al. 2023, ApJ, 957, 64
Spyromilio, J., Meikle, W. P. S., Learner, R. C. M., & Allen, D. A. 1988, Natur, 334, 327
Stritzinger, M., Valerin, G., Elias-Rosa, N., et al. 2023, TNSAN, 145, 1
Szalai, T., & Vinkó, J. 2013, A&A, 549, A79
Szalai, T., Vinkó, J., Könyves-Tóth, R., et al. 2019, ApJ, 876, 19
Teffs, J., Ertl, T., Mazzali, P., Hachinger, S., & Janka, H. T. 2020, MNRAS, 499, 730
Teja, R. S., Singh, A., Basu, J., et al. 2023, ApJL, 954, L12
Tinyanont, S., Kasliwal, M. M., Krafton, K., et al. 2019, ApJ, 873, 127
Tsuna, D., Fuller, J., & Lu, W. 2025, arXiv:2508.21116
Tucker, M. A., Shappee, B. J., Huber, M. E., et al. 2022, PASP, 134, 124502
Utrobin, V. P., Chugai, N. N., & Andronova, A. A. 1995, A&A, 295, 129
Van Dyk, S. D., Srinivasan, S., Andrews, J. E., et al. 2024b, ApJ, 968, 27
Van Dyk, S. D., Szalai, T., Cutri, R. M., et al. 2024a, ApJ, 977, 98
Vasylyev, S. S., Yang, Y., Filippenko, A. V., et al. 2023, ApJL, 955, L37
Virtanen, P., Gommers, R., Oliphant, T. E., et al. 2020, NatMe, 17, 261
Wooden, D. H., Rank, D. M., Bregman, J. D., et al. 1993, ApJS, 88, 477
Woosley, S. E., Heger, A., & Weaver, T. A. 2002, RvMP, 74, 1015
Yamanaka, M., Fujii, M., & Nagayama, T. 2023, PASJ, 75, L27
Yaron, O., Bruch, R., Chen, P., et al. 2023, TNSAN, 133, 1
Zapartas, E., de Mink, S. E., Justham, S., et al. 2021, A&A, 645, A6
Zhang, J., Lin, H., Wang, X., et al. 2023, SciBu, 68, 2548
Zimmerman, E. A., Irani, I., Chen, P., et al. 2024, Natur, 627, 759